Geochemistry, Geophysics, Geosystems

RESEARCH ARTICLE

10.1029/2018GC007586

Key Points:
- Correlation decreases with increasing core temperature, number of continents, internal heating, or decreasing reference viscosity
- Downwellings along continental margins increase thermal contrast between subcontinental and suboceanic mantle
- Decompression melting leads to basaltic crust production, which breaks the continents and destroys the correlation

Supporting Information:
- Supporting Information S1
- Data Set S1
- Movie S1
- Movie S2
- Movie S3
- Movie S4
- Movie S5
- Movie S6
- Movie S7
- Movie S8
- Movie S9
- Movie S10
- Movie S11
- Movie S12

Correspondence to:
C. Jain,
charitra1989@gmail.com

Citation:
Jain, C., Rozel, A. B., & Tackley, P. J. (2019). Quantifying the correlation between mobile continents and elevated temperatures in the subcontinental mantle. *Geochemistry, Geophysics, Geosystems*, *20*, 1358–1386. https://doi.org/10.1029/2018GC007586

Received 30 MAR 2018
Accepted 25 JAN 2019
Accepted article online 7 FEB 2019
Published online 11 MAR 2019
Corrected 15 MAR 2019

This article was corrected on 15 MAR 2019. See the end of the full text for details.

Quantifying the Correlation Between Mobile Continents and Elevated Temperatures in the Subcontinental Mantle

C. Jain[1,2], A. B. Rozel[1], and P. J. Tackley[1]

[1]Institute of Geophysics, Department of Earth Sciences, ETH Zurich, Zurich, Switzerland, [2]Now at Department of Earth Sciences, Durham University, Science Labs, Durham, United Kingdom

Abstract Continents influence the mantle's convective wavelength and the heat flow escaping from the planet's surface. Over the last few decades, many numerical and analytical studies have contributed to the debate about whether the continents can warm up the subcontinental mantle or not and if they do, then to what extent? However, a consensus regarding the exact nature and magnitude of this correlation between continents and elevated temperatures in the subcontinental mantle remains to be achieved. By conducting a systematic parameter study using 2-D global mantle convection simulations with mobile continents, we provide qualitative and quantitative observations on the nature of this correlation. In our incompressible and compressible convection models, we observe the general processes of downwellings bringing cold material into the mantle along continental margins and a subsequent buildup of warm thermal anomalies underneath the continents. We compute the amplitude and degree of this correlation using spectral decomposition of the temperature and composition fields. The dominant degree of correlation evolves with time and changes with continental configuration. Using simple empirical fits, we observe that this correlation decreases with increasing core temperature, number of continents, internal heating, or decreasing reference viscosity. We also report simple regressions of the time dependence of this correlation. Additionally, we show that decompression melting as a result of a mantle upwelling or small-scale sublithospheric convection leads to voluminous volcanism. The emplacement of this dense basalt-eclogite material breaks the continents apart and destroys the correlation.

1. Introduction

The existence of dynamic feedback between the convecting mantle and the drifting continents is evident from numerical simulations and laboratory experiments. It has been shown that continents exert a first-order influence on Earth's mantle flow by affecting convective wavelength and surface heat flow (e.g., Grigné et al., 2007; Gurnis, 1988; Guillou & Jaupart, 1995; Lowman & Jarvis, 1993, 1996; Lowman & Gable, 1999; Phillips & Bunge, 2005; Yoshida et al., 1999; Zhong & Gurnis, 1993; Zhong & Liu, 2016; Zhong et al., 2007). The notion that continents can have an insulating effect on the mantle has received considerable attention over the last few decades (Cooper et al., 2006, 2013; Lenardic & Moresi, 2001; Lenardic et al., 2005).

Numerical simulations by Gurnis (1988) and Zhong and Gurnis (1993) showed the accumulation of heat underneath mechanically stiff, thick continental plates, and the development of long-wavelength thermal structures in the mantle. By using laboratory experiments, Guillou and Jaupart (1995) proposed that continents wider than the mantle depth are susceptible to breakup as they generate large positive thermal anomalies below them. Lowman and Gable (1999) suggested that the inclusion of oceanic plates and internal heating in convection modeling reduces the thermal contrast between suboceanic and subcontinental mantle. By modeling mechanically and thermally distinct continental and oceanic plates, but with the same thickness and a depth-dependent viscosity, Heron and Lowman (2010, 2011) argued that continental insulation plays a minor role in affecting the mantle's thermal field and did not report any elevated temperatures in the subcontinental mantle on timescales relevant to supercontinent assembly. Heron and Lowman (2014) further highlighted the decreasing influence of continental insulation on subcontinental mantle temperatures with increasing Rayleigh number Ra, albeit with a stationary supercontinent and viscosity not being fully temperature-dependent in their models. In their mixed-heating (basal and internal) Cartesian models, O'Neill et al. (2009) showed the propensity of plumes to rise underneath continents (~3,000 km in extent) and elevate temperatures away from the cold slabs subducting along continental margins. This temperature anomaly diminishes with strongly temperature- dependent viscosity. Moreover, for continents over 8,000 km in width, the inefficient lateral advection of material underneath the continents results in the formation of drip instabilities causing small-scale convection cells and a reduction in the thermal anomaly. They also explored the possible relation between melting and rifting and did not observe voluminous volcanism owing to hot upwelling subcontinental mantle in their steady state simulations. By simulating mobile continents, Phillips and Coltice (2010) also observed an increase in subcontinental temperature as a function of both continental extent and convective wavelength, although their models lacked oceanic plates and a temperature-dependent viscosity, which might result in overestimation of the resulting temperature difference between suboceanic and subcontinental mantle. Based on their purely internally heated 3-D models with various continental configurations and width, Rolf et al. (2012) showed temperature excess of up to 140 K underneath the continents compared to the suboceanic mantle. They showed that as opposed to a dispersed configuration, a cluster of continents results in higher insulation and provides a possible explanation for the episodic continental crustal growth (Condie, 2004; Hawkesworth & Kemp, 2006; Pearson et al., 2007). The absence of basal heating and plumes in their models is a significant simplification and demands further testing.

Considering all these numerical studies with varying degrees of complexity, some underlying processes have been agreed upon. First, subcontinental mantle can become hotter than suboceanic mantle provided that subduction zones develop along continental margins and inhibit lateral mantle flow. Furthermore, for this transient thermal anomaly to develop, the continents would have to be stationary for a sufficient length of time. Second, any factors that promote thermal mixing will diminish the amplitude of these anomalies. Most of these studies have however neglected the effects of melting-induced crustal production (hereafter, referred to as MCP), which are considered as significant processes in planetary evolution and dynamics (e.g., Davies, 2007; Nakagawa & Tackley, 2012; Ogawa, 2014; Stevenson, 1990; Xie & Tackley, 2004b). Lourenço et al. (2016) have also shown that MCP strongly enhances the mobility of the lid and extends the range of parameters over which a mobile lid is present on planets. Aiming for more realistic simulations, we consider MCP in a subset of our simulations.

Understanding the mechanism behind the voluminous magmatism and the resulting formation of continental flood basalts (CFB) remains a contentious issue. Anderson (1982) proposed that the geoid highs above Africa and South Pacific were caused by elevated temperatures generated by the assembly of the Pangea supercontinent during the Mesozoic. Coltice et al. (2007, 2009) argued in favor of continental aggregation induced elevated temperatures and large-scale melting that caused the emplacement of continental flood basalts of the Central Atlantic Magmatic Province following the breakup of Pangea. Alternatively, it has been proposed that deep-seated mantle plumes can cause intense magmatic activity while emplacing CFB followed by continental breakup (Campbell & Griffiths, 1990; Condie, 2004; Morgan, 1972; Richards et al., 1989; Scrutton, 1973; White & McKenzie, 1989).

In this paper, we study the possible correlation between mobile continents and elevated subcontinental mantle temperatures using a broad range of thermochemical mantle convection simulations. We systematically vary parameters such as core-mantle boundary (CMB) temperature, continental configuration, mantle heating modes (internal and basal heating), and reference viscosity. We further investigate the effect of MCP on this correlation and explore the possible origin of CFB. We introduce the methodology and the governing equations in section 2. We present the results of our simulations in section 3 and discuss their geophysical implications in section 4. Finally, we summarize the key aspects of our study in section 5.

2. Physical Model and Numerical Model

We study the thermochemical evolution of the mantle coupled with mobile continents. Continents are simplified as homogeneous Archean cratons and represented by a continuous nondiffusive compositional field $C\,(0 \leq C \leq 1)\,(C = 1$ being pure continental and $C = 0$ being pure noncontinental material). In our models, these different cratons are allowed to drift closer and collide. They can then drift as a combined continent or move apart. We do not specify a distinct continental thermal conductivity. Compared to the ephemeral oceanic crust that reaches a maximum age of ~200 Myr, continents are much older (Rudnick & Gao, 2003). Geophysical, geochemical, and geological investigations have attributed continents' long-term stable behavior to the presence of strong, compositionally buoyant, and possibly viscous cratonic roots underlying the

Table 1
Nondimensional and Dimensional Parameters Used in This Study

Property	Symbol	Value	Units
Comp. yield stress ratio	$\Delta\tau_Y^C$	10	—
Comp. viscosity ratio	$\Delta\eta^C$	100	—
Reference density	ρ_0	3,300	kg/m^3
Density contrast	$\Delta\rho_{craton}$	−100	kg/m^3
Surface temperature	T_{surf}	300	K
Specific heat capacity	C_P	1,200	J/kg/K
Gas constant	R	8.3145	J/K/mol
Gravity	g	9.81	m/s^2
Mantle thickness	D	2,890	km
Surface thermal expansivity[a]	α	$3 \cdot 10^{-5}$	K^{-1}
Surface thermal diffusivity[a]	κ	$7.57 \cdot 10^{-7}$	m^2/s
Incompressible convection			
Surface yield stress	τ_Y^0	37	MPa
Initial potential temperature	T_{P0}	1550	K
Surface thermal conductivity[a]	k	3.0	W/m/K
Compressible convection with melting-induced crustal production			
Surface yield stress	τ_Y^0	40	MPa
Yield stress gradient	τ_Y'	0.005	—
Initial potential temperature	T_{P0}	1900	K
Surface thermal conductivity[a]	k	3.5	W/m/K
Reference viscosity	η_0	$1 \cdot 10^{20}$	Pa·s
Latent heat of melting	L	600	kJ/kg

Note. Parameters that vary with simulations are given in Table 4.
[a]Valid at the surface for olivine phase system.

continental crust (Boyd, 1987, 1989; Jordan, 1978, 1979; Hirth & Kohlstedt, 1996; Lee, 2003; Pollack, 1986; Schutt & Lesher, 2006). Accordingly, continents are modeled as lighter and more viscous than the mantle. We use models featuring both incompressibility (with nondimensional units) and compressibility (with dimensional units) with parameters listed in Table 1. The numerical model employed here incorporates pressure-temperature-dependence of viscosity, internal and basal heating, plasticity, phase transitions, diffusion creep, melting, and crustal production and is an extension of the ones described by Rolf and Tackley (2011) and Rolf et al. (2012).

2.1. Rheology

In our models, diffusion creep with homogenous grain size is the viscous deformation mechanism. Between continents and mantle material, the density contrast is specified by the buoyancy ratio B and the rheological contrast is controlled by viscosity ratio $\Delta\eta^C$ and yield stress ratio $\Delta\tau_Y^C$. The mantle is divided into three different layers i: upper mantle (1), lower mantle (2), and post-perovskite layer (3), with each layer having different values for activation energy E_i and activation volume V_i (Karato & Wu, 1993; Yamazaki & Karato, 2001). See Table 2 for a list of the rheological properties used in the study. The dimensional temperature-, pressure-, and composition-dependent viscosity η in each layer is given by an Arrhenius law:

$$\eta(T, P, C) = \eta_0 \Delta\eta_i \Delta\eta^C \exp\left(\frac{E_i + PV_i}{RT} - \frac{E_i}{RT_0}\right), \quad (1)$$

where η_0 is the reference viscosity at zero pressure and reference temperature T_0 (1600 K), $\Delta\eta_i$ is the viscosity offset between layer i and the reference viscosity, P is the pressure, R is the gas constant, and T is the dimensional absolute temperature; η_0 is valid for the phase system olivine and the reference composition (60% olivine and 40% pyroxene-garnet), both of which have viscosity multipliers of 1 (see Table 2).

Table 2
Rheological Properties Used for Compressible Convection in Three Different Layers i

Property	Symbol	Value	Units
Upper mantle (Olivine)			
Activation energy	E_1	300	kJ/mol
Activation volume	V_1	5.00	cm^3/mol
Pressure scale	P_1	∞	GPa
Viscosity multiplier	$\Delta\eta_1$	1.0	—
Lower mantle (Perovskite)			
Activation energy	E_2	370	kJ/mol
Activation volume	V_2	3.65	cm^3/mol
Pressure scale	P_2	200	GPa
Viscosity multiplier	$\Delta\eta_2$	30.0	—
Post-perovskite layer			
Activation energy	E_3	162	kJ/mol
Activation volume	V_3	1.40	cm^3/mol
Pressure scale	P_3	1610	GPa
Viscosity multiplier	$\Delta\eta_3$	0.1	—

Following the viscosity profile expected by the inversion of postglacial rebound data (Čížková et al., 2012) and geoid inversion studies (e.g., Ricard et al., 1989, 1993), a viscosity jump of 30 is applied at the upper-lower mantle transition (660 km). As suggested by mineral physics experiments and theoretical calculations (Ammann et al., 2010; Hunt et al., 2009), an additional viscosity jump of 0.1 (compared to reference viscosity) is imposed at the transition to post-perovskite at lowermost mantle depths (2,740 km). The activation volume decreases exponentially with increasing pressure in each layer i according to the relation:

$$V(P) = V_i \exp\left(-\frac{P}{P_i}\right), \tag{2}$$

where P_i is the pressure scale, which is different for each layer i as given in Table 2.

In simulations featuring incompressibility (nondimensional units), the viscosity takes the form:

$$\eta(T^*, C) = \Delta\eta^{C} \exp\left(\frac{\tilde{E}_A}{T^*+1} - \frac{\tilde{E}_A}{2}\right), \tag{3}$$

where $\Delta\eta^C = \eta(T^*, C=1)/\eta(T^*, C=0)$ accounts for the compositional dependence and $\tilde{E}_A = 2\ln(\eta(T^*=0, C)/\eta(T^*=1, C))$ is the nondimensional activation energy, which accounts for the temperature dependence of the viscosity. A constant value of 23.03 for $\tilde{E}_A$ gives 5 orders of magnitude viscosity variation in the interval of nondimensional temperature $0 \le T^* \le 1$. By adding an offset to the temperature, equation (3) is obtained from equation (1) using the relation:

$$\frac{E}{RT} = \frac{E}{R\left(T_{surf} + \Delta T\ T^*\right)} = \frac{E}{RT_{surf}} \frac{1}{\left(1 + \Delta T/T_{surf}\ T^*\right)} = \frac{\tilde{E}_A}{1+T^*}, \tag{4}$$

where T_{surf} is the surface temperature and ΔT is the temperature scale. In our case, as is often done in geodynamics, we simply considered that $T_{surf} = \Delta T$ and the nondimensional activation energy is defined by $\tilde{E}_A = E/\left(RT_{surf}\right)$. This approximation might seem quite strong but what matters is the viscosity contrast more than the exact shape of the viscosity profile.

To break the stagnant lid and obtain Earth-like plate tectonics, plastic yielding is assumed to be the weakening mechanism (Moresi & Solomatov, 1998; Tackley, 2008b). The maximum stress that a material can sustain before deforming plastically is given by the yield stress τ_Y, and it increases linearly with depth d at a rate of τ'_Y,

10.1029/2018GC007586

$$\tau_\mathrm{Y}(d, C) = \Delta\tau_\mathrm{Y}^\mathrm{C}\left(\tau_\mathrm{Y}^0 + d\tau'_\mathrm{Y}\right), \tag{5}$$

where $\Delta\tau_\mathrm{Y}^\mathrm{C} = \tau_\mathrm{Y}(d, C = 1)/\tau_\mathrm{Y}(d, C = 0)$ accounts for the different yield stresses of continental and oceanic lithosphere; $\tau_\mathrm{Y}^0 = \tau_\mathrm{Y}(d = 0, C = 0)$ is the yield stress at the oceanic surface. If the convective stresses exceed the yield stress, the viscosity is reduced to the yielding viscosity $\eta_\mathrm{Y} = \tau_\mathrm{Y}/2\dot{\epsilon}$, where $\dot{\epsilon}$ is the second invariant of the strain-rate tensor. The effective viscosity is then given by

$$\eta_\mathrm{eff} = \left(\frac{1}{\eta} + \frac{2\dot{\epsilon}}{\tau_\mathrm{Y}}\right)^{-1}. \tag{6}$$

In simulations with MCP, the viscosity is limited between 10^{18} and 10^{25} Pa·s to mitigate large viscosity variations, which would decrease the stability of the code. These viscosity cutoffs are reached at temperatures of ~1150 K (highest viscosity) and ~5900 K (lowest viscosity). We therefore resolve the viscosity of the mantle through the entire evolution of the Earth.

Continents are less dense by $\Delta\rho_\mathrm{craton} = -100\ \mathrm{kg/m^3}$ (buoyancy ratio $B = \Delta\rho_\mathrm{craton}/(\alpha\rho_0\Delta T) = -0.4$ with thermal expansivity α, reference density ρ_0, and temperature scale ΔT) compared to the mantle. A viscosity ratio $\Delta\eta^\mathrm{C} = 100$ and yield stress ratio $\Delta\tau_\mathrm{Y}^\mathrm{C} = 10$ are used to ensure cratonic lithosphere's relative stability and longevity when compared to oceanic lithosphere. When considering nondimensional units, yield stresses τ_Y are nondimensionalized with the factor $\eta_0\kappa/D^2$. The dimensional time t is obtained from the dimensionless time t^* using $t = t^* D^2/\kappa$ and similarly, velocities v are obtained from dimensionless velocities v^* using $v = v^*\kappa/D$.

The potential correlation between continents and temperature in the subcontinental mantle is strongly related to mantle stirring. However, as we use different values of reference viscosity in models with incompressibility, the average number of overturns occurring in the mantle decreases for cases with higher viscosity for a given amount of dimensional time. To overcome this issue, we use a renormalized time t_r based on the average dimensional velocity of our simulations. The renormalized time is given by

$$t_\mathrm{r} = \frac{v_\mathrm{E}}{< v >_t} t, \tag{7}$$

with

$$< v >_t = \frac{1}{t^*_\mathrm{max}} \int_{t^*=0}^{t^*=t^*_\mathrm{max}} v_\mathrm{RMS}\, \mathrm{d}t^*, \tag{8}$$

where v_RMS is the dimensional root-mean-square (RMS) velocity in the whole domain and v_E is the average plate velocity for present-day Earth (3.4 cm/year as used in Coltice et al., 2012, considering a transit time of 85 Myr for present-day Earth's mantle); t^*_max is the final dimensionless time in our simulations. We thus force a sufficiently large number of overturns in all cases, which leads to comparable evolution states. This renormalization is not required for models with compressibility and dimensional units.

2.2. Conservation Equations, Boundary Conditions, and Solution Method

Using the code StagYY (Tackley, 2008a), we solve the equations for both incompressible (Boussinesq approximation) and compressible (anelastic approximation with infinite Prandtl number) Stokes flow. The equations of conservation of mass, momentum, and energy governing compressible flow are (see Chandrasekhar, 1961; Schubert et al., 2001, for details):

$$\frac{\partial}{\partial x_j}\left(\rho v_j\right) = 0, \tag{9}$$

$$0 = -\frac{\partial P}{\partial x_i} + \frac{\partial}{\partial x_j}\left\{\eta\left(\frac{\partial v_i}{\partial x_j} + \frac{\partial v_j}{\partial x_i} - \frac{2}{3}\delta_{ij}\frac{\partial v_k}{\partial x_k}\right)\right\} + \rho g_i, \tag{10}$$

$$\rho C_P\left(\frac{\partial T}{\partial t} + \mathbf{v}\cdot\nabla T\right) - \alpha T\left(v_r \cdot \nabla_r P\right) = \nabla\cdot\left(k\nabla T\right) + \frac{\partial v_i}{\partial x_j}\sigma_{ij} + \rho H, \tag{11}$$

with density ρ, position x_j ($j = 1, 2, 3$ hereinafter), velocity component v_j, Kronecker delta δ_{ij}, gravity g, specific heat capacity C_P, thermal expansivity α, thermal conductivity k, stress tensor σ_{ij}, and internal heating

10.1029/2018GC007586

Table 3
Phase Change Parameters for Olivine and Pyroxene-Garnet Phase Systems

Depth (km)	Temperature (K)	$\Delta\rho$ (kg/m^3)	γ (MPa/K)
Olivine ($\rho_s = 3,240$ kg/m^3)			
410	1600	180	2.5
660	1900	400	−2.5
2,740	2300	61.6	10
Pyroxene-garnet ($\rho_s = 3,080$ kg/m^3)			
60	1000	350	0
400	1600	150	1
720	1900	400	1
2,740	2300	61.6	10

Note. ρ_s is the surface density at zero pressure, $\Delta\rho$ is the density jump across a phase transition, and γ is the Clapeyron slope.

rate per unit mass H (when specified). The reader is referred to Rolf et al. (2012) for equations describing incompressible flow.

We use a 2-D spherical annulus geometry (Hernlund & Tackley, 2008) with a varying radial resolution and the domain is discretized by 768 (lateral) times 64 (radial) cells. 4,915,200 tracers are advected through the domain using a fourth-order Runge-Kutta method and converted to a continuum compositional field using the tracer-ratio method (Tackley & King, 2003; 983,040 tracers in compressible convection calculations). This represents an average of 100 tracers per cell for the incompressible convection simulations and 20 tracers per cell for the simulations considering compressibility and MCP. However, in the latter case, the surface cells are typically replenished with tracers due to magmatism, which results in a local increase of tracer density. We employ free-slip boundary conditions for the surface and the CMB with the surface temperature fixed as 300 K. In models featuring compressibility, core cooling is included with a parameterization based on Buffett et al. (1992, 1996) and for the parameterization details, the reader is referred to Nakagawa and Tackley (2004). The code uses a finite volume discretization, with velocity and pressure defined on a staggered grid. For incompressible convection calculations, a multigrid solver is used. For compressible convection calculations, a parallel MUMPS solver from the PETSc package is used (Amestoy et al., 2000).

2.3. Phase Changes and Composition

The model includes a parameterization based on mineral physics data (Irifune & Ringwood, 1993; Ono et al., 2001) in which minerals are divided into olivine and pyroxene-garnet systems that undergo solid-solid phase transitions, as used in previous studies (Nakagawa & Tackley, 2012; Xie & Tackley, 2004b). Their mixture depends on the chemical composition, which varies between basalt (100% pyroxene-garnet) and harzburgite (75% olivine and 25% pyroxene-garnet). The mantle is initialized with a pyrolytic composition, which is taken as a petrological mixture of 80% harzburgite and 20% basalt (e.g., as in Xu et al., 2008). The phase change parameters are given in Table 3. At a depth of 60 km, basalt forms eclogite, which is around 190 kg/m^3 denser than olivine. At lowermost mantle depths, the phase transition from perovskite to post-perovskite is also considered (e.g., Tackley et al., 2013).

2.4. Melting and Crustal Production

When melting is considered, melt-induced differentiation changes the composition following previous work by Lourenço et al. (2016), Nakagawa et al. (2010), and Xie and Tackley (2004b). The composition and temperature fields are stored and advected on tracers. As melting is calculated on a cell level to ensure numerical efficiency, the cell-based solid composition and melt fraction are computed at cell centers using mass averaging of these tracers. At each time step, the required change in melt fraction for every cell is computed by comparing cell temperature T_{cell} with the composition-dependent pyrolite solidus T_{sol} (as used by Nakagawa & Tackley, 2004). The solidus temperature is a function fitting experimental data by Herzberg et al. (2000) in the upper mantle and by Zerr et al. (1998) in the lower mantle, which is increased linearly by up to 60 K as the basaltic component is depleted, with no melting possible once the basaltic component has been completely removed. In case the cell temperature exceeds or is lower than the solidus, then either more melt is generated or the existing melt is frozen in the cell to bring the cell temperature back to the solidus. Latent

Table 4
Simulations Featuring Incompressibility With Core Temperature T_{cmb} (K), Radiogenic Heating H (W/kg), Cratonic Thickness d_{craton} (km), Reference Viscosity η_0 (Pa·s), Number of Continents n_{craton}, Final Model Runtime t_r (Gyr), Average Velocity v_{RMS} (cm/year), Mean Surface Heat Flow Q_{surf} (TW), Mean CMB Heat Flow Q_{cmb} (TW), Dominant Degree of Correlation deg, Its Amplitude Corr (K), and the Averaged Evolution of the Correlation $\langle \partial corr/\partial t \rangle$ (K/Gyr)

T_{cmb}	H	η_0	n_{craton}	d_{craton}	t_r	v_{RMS}	Q_{surf}	Q_{cmb}	deg	Corr	$\langle \partial corr/\partial t \rangle$
2000[a,b]	0	$7.88 \cdot 10^{22}$	1	570	4.50	0.06	2.17	2.01	—	—	—
2000[b]	0	$7.88 \cdot 10^{22}$	2	570	4.14	0.05	2.14	1.96	—	—	—
2000[b]	0	$7.88 \cdot 10^{22}$	6	570	3.84	0.04	1.96	1.80	—	—	—
3000[c]	0	$7.88 \cdot 10^{22}$	1	570	4.50	0.46	12.57	11.78	1	231.24	11.53
3000[c]	0	$7.88 \cdot 10^{22}$	2	570	3.60	0.40	12.67	11.55	2	55.89	13.84
3000[a]	0	$7.88 \cdot 10^{22}$	3	570	4.50	0.39	13.74	12.08	3	3.57	37.14
3000	0	$7.88 \cdot 10^{22}$	4	570	4.50	0.35	14.10	12.66	1	17.38	21.17
3000[b]	0	$7.88 \cdot 10^{22}$	5	570	4.50	0.33	14.14	12.86	—	—	—
3000[b]	0	$7.88 \cdot 10^{22}$	6	570	4.50	0.26	13.72	12.91	—	—	—
4000[c]	0	$7.88 \cdot 10^{22}$	1	570	4.50	1.81	31.67	34.61	2	10.02	43.62
4000	0	$7.88 \cdot 10^{22}$	2	570	4.50	1.50	33.26	35.34	2	9.78	45.35
4000	0	$7.88 \cdot 10^{22}$	6	570	2.69	1.29	31.06	36.19	1	7.29	37.07
2000[b,d]	0	$7.88 \cdot 10^{22}$	2	570	2.23	0.05	2.62	2.22	—	—	—
3000[c,d]	0	$7.88 \cdot 10^{22}$	2	570	2.93	0.36	13.22	11.63	1	65.81	15.83
4000[b,d]	0	$7.88 \cdot 10^{22}$	2	570	0.89	1.03	31.57	32.88	—	—	—
3000	$3 \cdot 10^{-12}$	$7.88 \cdot 10^{22}$	1	570	4.50	1.08	20.25	12.40	1	75.71	17.47
3000	$3 \cdot 10^{-12}$	$7.88 \cdot 10^{22}$	2	570	4.50	0.78	21.25	13.09	2	20.84	20.06
3000	$3 \cdot 10^{-12}$	$7.88 \cdot 10^{22}$	6	570	4.50	0.74	21.64	13.75	1	14.47	22.02
3000[b]	$3 \cdot 10^{-12}$	$1.57 \cdot 10^{22}$	1	335	1.60	1.57	24.79	19.39	—	—	—
3000	$3 \cdot 10^{-12}$	$1.57 \cdot 10^{22}$	2	335	4.50	1.67	28.23	20.61	2	14.98	34.23
3000	$3 \cdot 10^{-12}$	$1.57 \cdot 10^{22}$	6	335	4.50	1.77	27.75	20.97	2	3.84	41.34
3000	$3 \cdot 10^{-12}$	$7.88 \cdot 10^{21}$	1	263	4.50	2.35	29.83	23.12	1	18.34	42.12
3000	$3 \cdot 10^{-12}$	$7.88 \cdot 10^{21}$	2	263	4.50	2.24	29.16	23.38	2	6.40	44.77
3000	$3 \cdot 10^{-12}$	$7.88 \cdot 10^{21}$	6	263	4.50	2.49	29.09	24.08	1	5.67	48.08
3000[c]	$6 \cdot 10^{-12}$	$7.88 \cdot 10^{22}$	1	570	4.50	1.88	26.52	13.20	1	54.78	27.90
3000	$6 \cdot 10^{-12}$	$7.88 \cdot 10^{22}$	2	570	4.50	1.13	29.55	14.01	2	28.24	28.43
3000	$6 \cdot 10^{-12}$	$7.88 \cdot 10^{22}$	6	570	4.50	1.29	29.49	14.71	6	−3.76	34.58
3000	$6 \cdot 10^{-12}$	$1.57 \cdot 10^{22}$	1	335	4.50	2.42	33.56	20.32	1	20.70	41.95
3000	$6 \cdot 10^{-12}$	$1.57 \cdot 10^{22}$	2	335	4.50	2.39	34.53	21.19	2	9.33	52.56
3000	$6 \cdot 10^{-12}$	$1.57 \cdot 10^{22}$	6	335	4.50	2.80	31.67	21.21	2	2.41	58.16
3000[a]	$6 \cdot 10^{-12}$	$7.88 \cdot 10^{21}$	1	263	4.50	3.05	35.74	23.70	1	17.79	59.39
3000	$6 \cdot 10^{-12}$	$7.88 \cdot 10^{21}$	2	263	4.50	2.99	36.73	24.30	2	5.64	48.99
3000	$6 \cdot 10^{-12}$	$7.88 \cdot 10^{21}$	6	263	4.50	3.44	35.82	24.83	1	6.29	52.72

Note. For correlation, temperature field was averaged in the depth window w_{T1} for all simulations.
[a]Additional cases presented in Figures A1 –A3 (s1–s3). [b]Unrealistic cases excluded from empirical regressions. See text for details. [c]Cases presented in section 3.1.1 and Figures 2 –4 (a–e). [d]Continents initialized 90° apart.

heat of melt is consumed during melting and released during freezing and the resulting change in temperature ΔT_{cell} is computed for each cell. Accordingly, molten basaltic tracers are created in each cell. If the melt generated on tracers is at less than 300 km depth, it is instantaneously removed and erupted at the surface by transporting the tracers. The erupted melt is further solidified to generate oceanic crust with the surface temperature (Christensen & Hofmann, 1994; Xie & Tackley, 2004a). This is equivalent to considering a much shorter time scale of melt migration than that of the mantle flow (Kelemen et al., 1997).

2.5. Criterion for Correlation

To investigate whether there is a correlation between continents and elevated temperatures in the subcontinental mantle, we perform Fourier decompositions of both temperature T and composition C fields. The

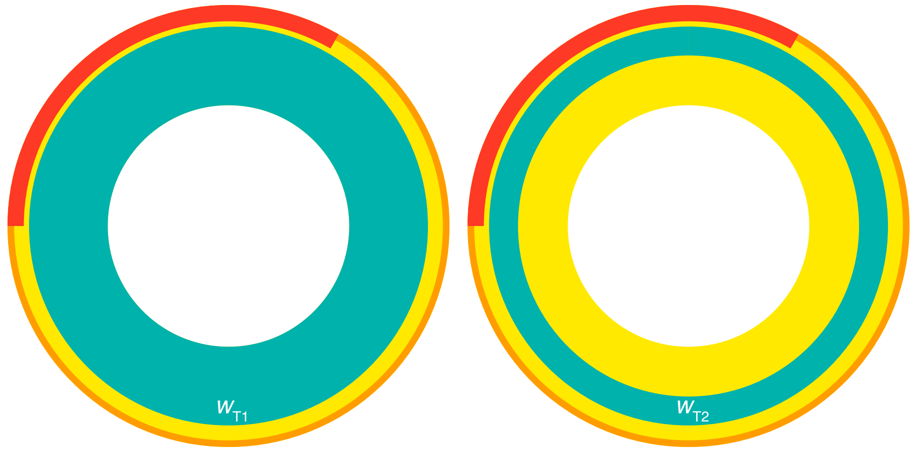

Figure 1. Schematic representation of the model with continent (red), composition correlation window (orange), and temperature correlation windows w_T (teal) as defined in section 2.5 (not to scale).

Fourier coefficients $a_{l,\mathrm{f}}$ and $b_{l,\mathrm{f}}$ of field f for harmonic degree l are given by

$$a_{l,\mathrm{f}} = \frac{1}{\pi\left(d_2 - d_1\right)} \int_{\theta=0}^{2\pi} \int_{d_1}^{d_2} f\left(\theta, R\right) \cos\left(l\theta\right) \mathrm{d}R\, \mathrm{d}\theta, \tag{12}$$

$$b_{l,\mathrm{f}} = \frac{1}{\pi\left(d_2 - d_1\right)} \int_{\theta=0}^{2\pi} \int_{d_1}^{d_2} f\left(\theta, R\right) \sin\left(l\theta\right) \mathrm{d}R\, \mathrm{d}\theta, \tag{13}$$

where d_1 and d_2 are the heights (measured from the base of the mantle) between which the temperature and composition fields are averaged. For the composition field, the Fourier coefficients are obtained by averaging in the top 100 km of the mantle: $d_2 - d_1 = 2,890 - 2,790 = 100$ km. The spectral decomposition of the temperature field is computed from 70 km below the continent (the same depth is employed below the oceans) to the CMB: $d_1 = d_\mathrm{craton} + 70$ where d_craton is given in Table 4. As the continental material can deform and break apart at its edges, it could sink underneath the existing continents and give a false positive correlation in our calculations. Hence, we consider the temperature field from below a fixed distance of 70 km irrespective of continental thickness. Two different depth windows are used: $w_\mathrm{T1} = 2,890 - d_1$ for the whole mantle, and $w_\mathrm{T2} = 1,000 - d_1$ for the upper part of the mantle. See Figure 1 for a schematic representation of the model setup.

Using Fourier coefficients, we calculate the correlation function between the temperature T and composition C fields using the relation:

$$\mathrm{corr}_{l,\mathrm{C,T}} = \left(a_{l,\mathrm{C}} a_{l,\mathrm{T}} + b_{l,\mathrm{C}} b_{l,\mathrm{T}}\right) \frac{\pi \Delta T}{\sum_{j=1}^{l} 2/j}, \tag{14}$$

where $\Delta T = 2500$ K is a constant used to dimensionalize temperature. The factor on the right-hand side of equation (14) is used to obtain the amplitude of the temperature anomalies assuming discontinuous continents. This formulation helps in computing the amplitude of a degree l sinusoidal thermal anomaly below a Heaviside-shaped continent of identical degree.

2.6. Time Dependence of the Correlation

The time dependence of the continent-temperature correlation can also be obtained using our spectral analysis. However, the result might not directly answer the question of how fast temperature can rise below a continent as the Fourier decomposition simultaneously reports how fast the regions away from the continents cool. Yet this spectral method gives insightful trends concerning the evolution of lateral temperature anomalies associated with the surface distribution of continents on a global scale.

Since the correlation has the dimensions of temperature, one can calculate the evolution of the lateral temperature anomalies for each harmonic degree. In the present study, we computed an average of the evolution

Table 5
Simulations Featuring Compressibility With Melting-Induced Crustal Production and Without Internal Heating. The final model runtime $t_r = 4.5$ Gyr for all simulations with Initial core temperature T_{cmb} (K), number of continents n_{craton}, depth window for averaging temperature field w_T, average velocity v_{RMS} (cm/yr), mean surface heat flow Q_{surf} (TW), mean core-mantle boundary heat flow Q_{cmb} (TW), dominant degree of correlation deg, its amplitude corr (K), the averaged evolution of the correlation $\langle \partial corr/\partial t\rangle$ (K/Gyr), reference viscosity $\eta_0 = 1{\cdot}10^{20}$ Pa·s and cratonic thickness $d_{craton} = 231$ km

$T_{\rm cmb}$	$n_{\rm craton}$	$w_{\rm T}$	$v_{\rm RMS}$	$Q_{\rm surf}$	$Q_{\rm cmb}$	*deg*	Corr	$\langle \partial{\rm corr}/\partial t\rangle$
3500	1	1	1.19	16.35	5.85	1	38.86	24.22
3500[a]	1	2	0.91	13.12	5.45	1	17.32	74.22
3500	2	1	0.89	12.63	5.68	1	56.06	27.76
3500	2	2	0.94	13.04	5.92	2	20.30	42.73
4000	1	1	2.03	18.40	12.59	1	19.62	62.78
4000[a,b]	1	2	1.74	17.48	13.17	1	28.08	89.76
4000	2	1	1.52	17.77	13.31	2	13.26	59.89
4000	2	2	2.01	16.68	12.03	2	0.07	65.41
4500	1	1	1.48	18.58	13.23	7	−3.05	46.29
4500[a]	1	2	1.50	19.02	13.33	1	23.52	85.67
4500	2	1	1.50	16.97	13.30	9	−5.47	41.89
4500	2	2	1.49	19.31	12.95	2	5.95	79.38

[a]Cases f–h. [b]Case presented in Figure 5.

of temperature anomalies over the first 6 degrees only to avoid introducing too much noise. Thus, we used the following:

$$\langle \frac{\partial \mathrm{corr}_{C,T}}{\partial t} \rangle = \frac{1}{N} \sum_{l=1}^{N} \frac{1}{t_{\max}} \int_{t=0}^{t_{\max}} \left| \frac{\partial \mathrm{corr}_{l,C,T}}{\partial t} \right| \mathrm{d}t, \tag{15}$$

where N is the number of harmonics used for the average ($N = 6$ in the present study) and $t_{\max}$ is the final physical time nonrenormalized by the average velocity.

3. Results

In order to investigate both the magnitude of temperature anomalies appearing below continents (together with the heating or cooling at a distance from continents) and their effects on mantle convection, we performed two sets of simulations. First, we examined 33 cases considering incompressible convection with constant basal and internal heating (Table 4). Second, we performed 12 simulations considering compressible convection with core cooling, no internal heating, melting, and crustal production (Table 5). For both sets of simulations, the surface heat flow $Q_{\rm surf}$ and CMB heat flow $Q_{\rm cmb}$ reported in this paper are obtained by multiplying the heat fluxes obtained in 2-D simulations by the surface area of the Earth. The heat flows can therefore be directly compared to Earth's values.

The absence of melting, and thereby the lack of consumption of latent heat in the first set of simulations allows the mantle temperatures to rise. Thus, we were able to study the effect of core temperature $T_{\rm cmb}$, number of continents $n_{\rm craton}$, radiogenic heating H, and reference viscosity η_0 on the amplitude of these thermal anomalies. In cases with melting and crustal production, we also observed the development of warm thermal anomalies below the continents, which often caused their breakup.

3.1. First Set of Simulations: Incompressible Convection Without MCP

In this set of simulations, we systematically varied the following parameters (see Table 4):

- constant internal heating: $H = 0$, $3{\cdot}10^{-12}$, and $6{\cdot}10^{-12}$ W/kg,
- constant core temperature: $T_{\rm cmb} = 2000$, 3000, and 4000 K,

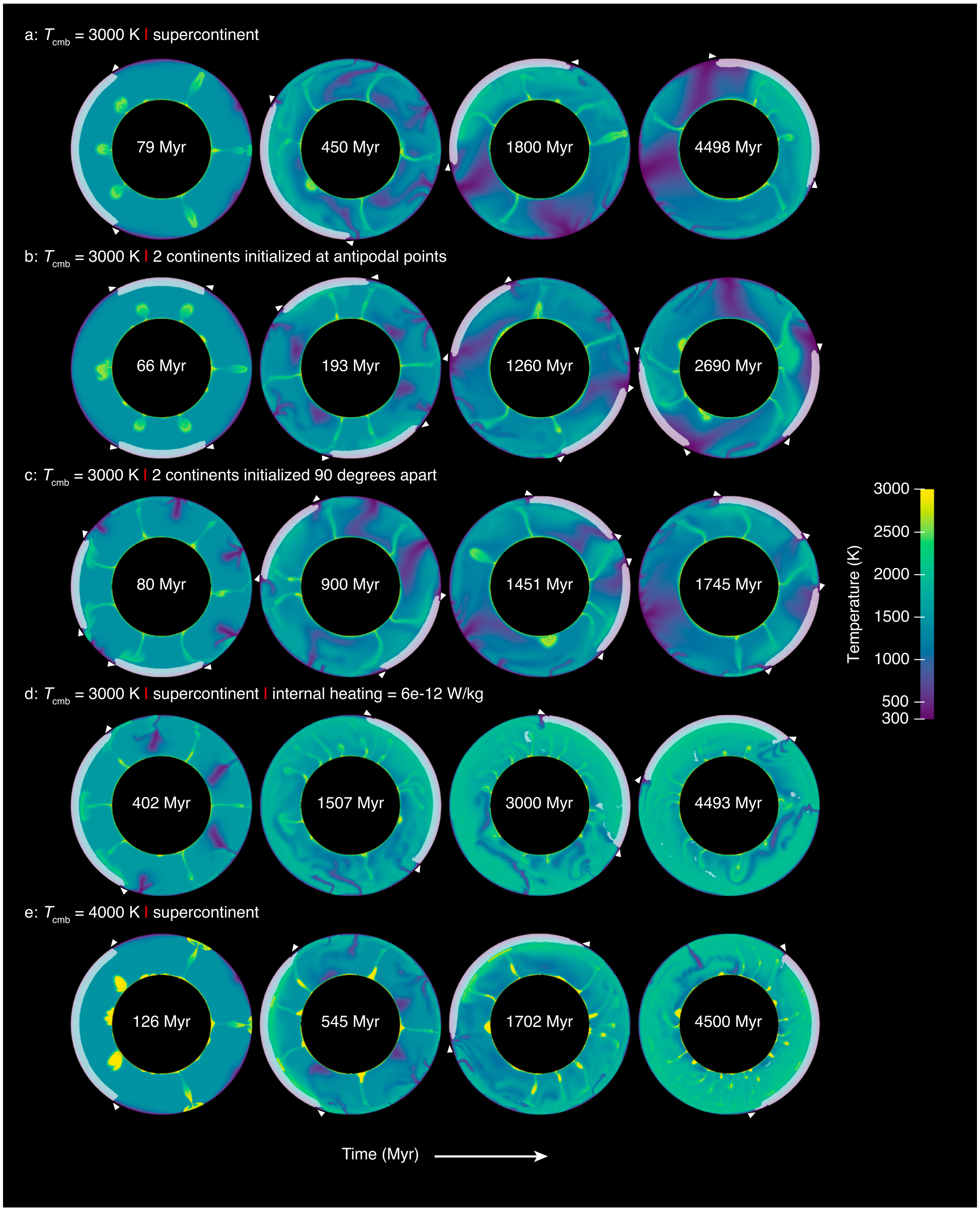

Figure 2. Thermal evolution of the cases a–e featuring incompressibility and without melting-induced crustal production. White triangles demarcate the continents, which are represented by composition field (white) superimposed over the temperature field. A small thermal anomaly of 125 K is introduced in the mid-mantle at 3 o'clock in all these models.

- initial number of continents: 1, 2, and 6, where the sum of the continents' length is always 30% of the surface length,
- initial position of continents: antipodal points and 90° apart,
- reference viscosity: $\eta_0 = 7.88 \cdot 10^{21}$, $1.57 \cdot 10^{22}$, and $7.88 \cdot 10^{22}$ Pa·s (see Table 1 for all parameters).

The thickness of continents is decided in accordance with the expected background lithospheric thickness as cratons on Earth have a larger thickness than the oceanic lithosphere. Boundary layer theory (Solomatov,

1995) demonstrates that self-consistently forming boundary layers depend on the Rayleigh number Ra: $\delta \simeq D\mathrm{Ra}^{-1/3}$, where δ is the lithospheric thickness and D is the mantle thickness. The Rayleigh number itself depends on several quantities that are kept fixed in our simulations but also on the core to surface temperature difference and the internal viscosity. For simplicity, since we vary the core temperature much less than the viscosity in our parameter space, we chose to only use a viscosity-dependent continent thickness. Assuming an oceanic boundary layer thickness of $\delta_{\mathrm{oceanic,E}} = 100$ km and continental boundary layer thickness of $\delta_{\mathrm{craton,E}} = 210$ km for the Earth, our oceanic and continental initial lithosphere thicknesses are obtained using the relation $\delta_{\mathrm{model}} = \left(\eta/\eta_E\right)^{1/3} \cdot \delta_{\mathrm{E}}$ as used previously in Rolf and Tackley (2011). This ensures that the continents are always thicker than the surrounding lithosphere for any choice of reference viscosity. A small thermal perturbation of 125 K is introduced in the mid-mantle at 3 o'clock to help initiate the first upwellings. In this set of simulations, a value of 1550 K is used for initial potential temperature T_{P0}, which represents the temperature of a given portion of the mantle if it ascended adiabatically to the surface without undergoing melting (McKenzie & Bickle, 1988).

3.1.1. Qualitative Observations

Figures 2 –4 depict the temporal evolution of five cases to help understand why and how positive temperature anomalies tend to be located below continents. Figure 2 shows the evolution of the temperature fields, and Figure 3 represents the evolution of the correlation between temperature and composition field (cratons) for harmonic degrees 1 to 10. Figure 4 shows the time series of CMB heat flow Q_{cmb}, surface heat flow Q_{surf}, and the fraction of internal heating $(Q_{\mathrm{surf}} - Q_{\mathrm{cmb}})/Q_{\mathrm{surf}}$. The rows of these three figures are organized as follows:

- a: 3000 K, one supercontinent, no internal heating;
- b: 3000 K, two continents initially at antipodal points, no internal heating;
- c: 3000 K, two continents initially 90° apart, no internal heating;
- d: 3000 K, one supercontinent, strong internal heating ($H = 6 \cdot 10^{-12}$ W/kg);
- e: 4000 K, one supercontinent, no internal heating.

All five cases employ a reference viscosity of $7.88 \cdot 10^{22}$ Pa·s.

In cases a–e, the initial plumes rising from the CMB are slower below the continents. Away from the continents, the oceanic lithosphere is weak enough to subduct and it brings cold material down into the lower mantle. This increases the thermal contrast between the surrounding mantle and regions of plume generation and provides additional buoyancy to the plumes, which quickly diffuse their heat while reaching the surface. As the continents are 100 times more viscous and have 10 times the yield stress compared to the oceanic lithosphere, they do not break. The thermal contrast between the subcontinental and suboceanic mantle is enhanced by the cold downwellings along continental margins and in regions away from the continents.

In case a presented in Figure 2a, the correlation between continent and temperature field arises as soon as convection cells form due to the strength of the cratonic material and this correlation is maintained throughout the simulation with a maximum amplitude of 237 K.

Additionally, cases b and c with two continents (each covering 15% of surface area) initialized at antipodal points and 90° apart are also presented in Figures 2b and 2c, respectively. When the two continents are at antipodal points, a degree-2 thermal structure is dominant in the mantle (Figures 2b and 3b) with an episode of anticorrelation in degree-2 between 1 and 1.5 Gyr of evolution. This anticorrelation can be understood by looking at the third column of Figure 2b, which shows that downwellings can be pushed to the edges of the continents and produce cold anomalies below the continents. In Figures 2c and 3c, continents are first closer to each other until 500 Myr, which generates a degree-1 correlation. They drift apart and form a degree-2 correlation until 1.3 Gyr and then come close again, which brings the correlation back to degree-1. These cases show that thermal structure of the mantle, and the degree of the continent-temperature correlation follows the geometrical configuration of the cratons.

In internally heated case d presented in Figure 2d, radiogenic heating strongly increases the internal temperature with time as melting and crustal production is not employed in this simulation. For Earth, the internal temperature would be buffered by the removal of latent heat resulting from MCP. Still, one can see that downwellings preferentially stay away from continents despite the nonstationarity of the flow patterns and the efficient stirring. Correlation in degree-1 and degree-2 is observed (see also Figure 3d).

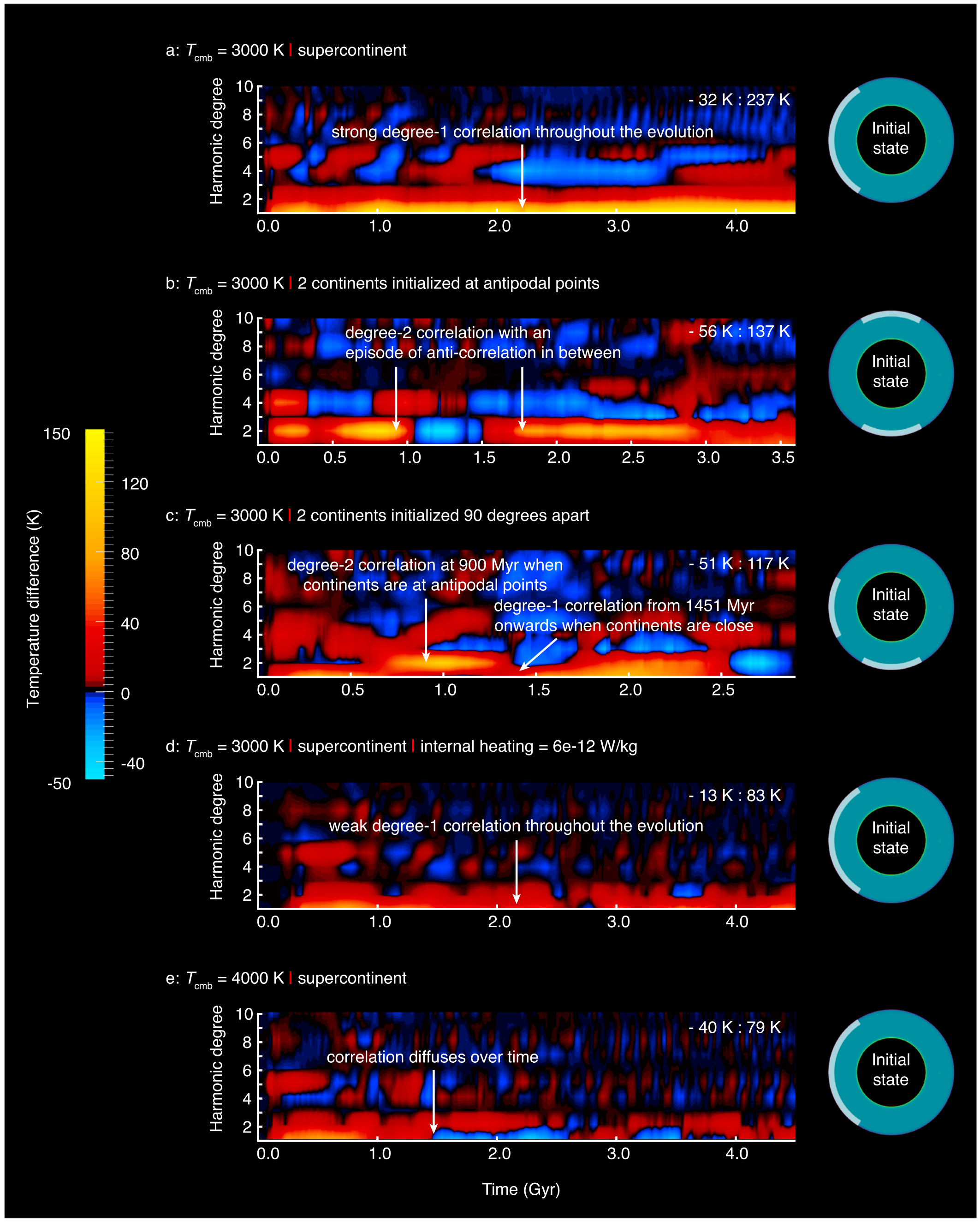

Figure 3. (left) Spectrogram of the cases a–e featuring incompressibility and without melting-induced crustal production, where positive (red to yellow) and negative (shades of blue) values indicate correlation and anticorrelation between continental material at the surface and elevated temperatures underneath, respectively (using temperature correlation window w_{T1}). Also shown are the minimum and maximum temperature contrasts obtained from the models. (right) Initial state of the models with continents (white).

In case e shown in Figure 2e, despite the fact that a degree-1 correlation is formed, the large core temperature generates strong plumes, which tend to push the continent laterally. This explains why the continent moves over a cold region (third column) and generates an anticorrelation (see arrow in Figure 3e).

As seen in the second column of each row of Figure 2, downwellings preferentially propagate through the lower mantle, also below continents, but the subcontinental upper mantle stays warm. This observation lead us to investigate the correlation using both the whole mantle and the upper part of mantle in the second

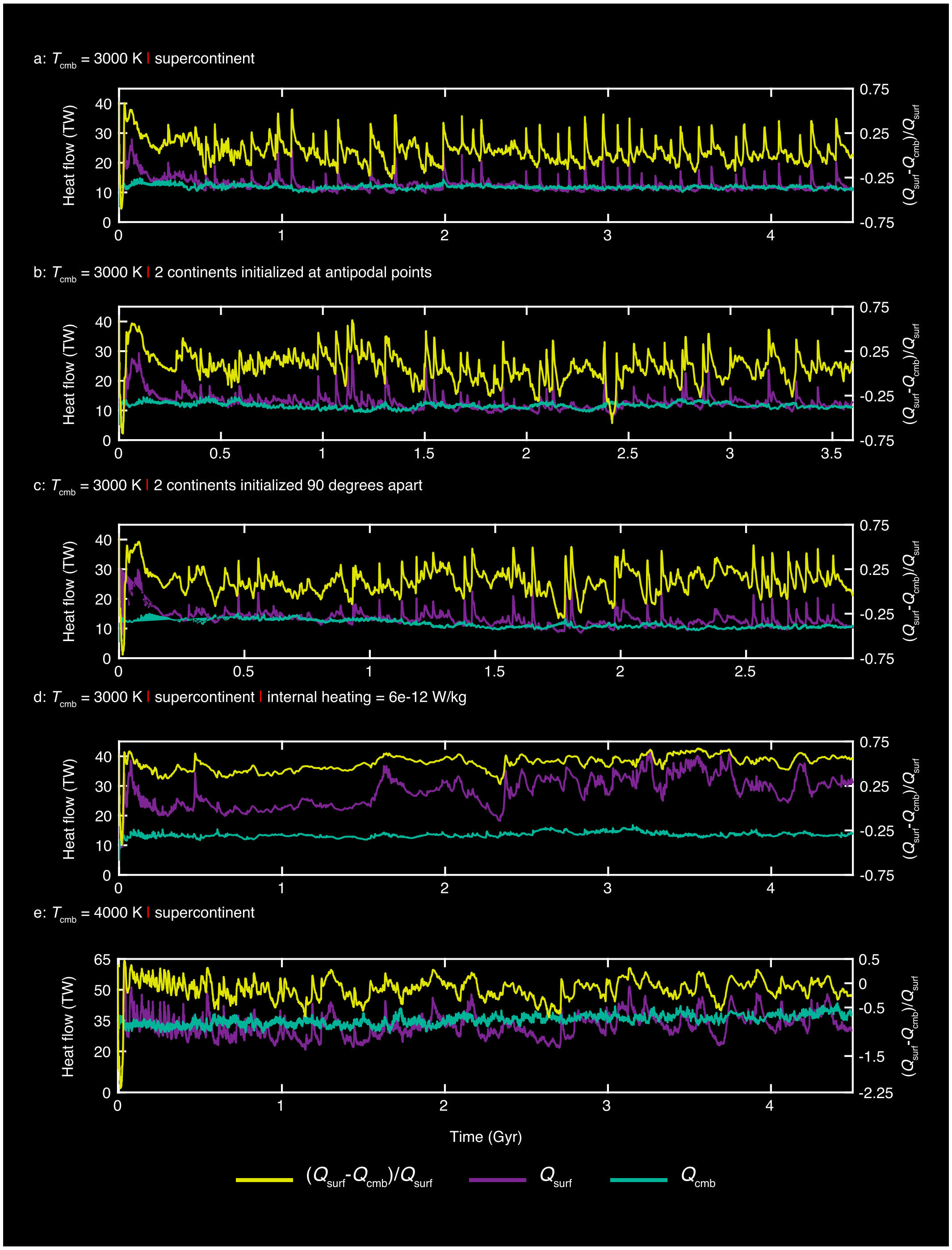

Figure 4. Time series of heat flow at the core-mantle boundary Q_{cmb} and at the surface Q_{cmb} on the left y axis for the cases a–e featuring incompressibility and without melting-induced crustal production. Also shown on the right axis is the fraction of internal heating $(Q_{surf} - Q_{cmb})/Q_{surf}$ as a function of time. Note that case e has different limits on both y axes.

set of simulations (see Figure 1 and rows 3 and 6 in Table 6). Despite the known limitations of numerical models, this observation is probably robust and applies to the Earth. Even if slabs rebound at the 660 km discontinuity on Earth, they do not tend to come back up below cratons due to their weight.

3.1.2. Effects of the Reference Viscosity and Internal Heating Rate

Figures 2d and 3d show that a degree-1 correlation below a supercontinent persists with strong internal heating but is lower in amplitude. We observe that a decrease in reference viscosity (see Figures A1s3 and A2s3)

Table 6
Empirical Regressions of the Continent-Temperature Correlation (K) and Their Evolution (K/Gyr)

Incompressible convection-no melting			Stand. Dev.
$\ln\left(\mathrm{corr}_{i,\mathrm{C,T}} - 6.944\right)$	$=$	$0.732 - 2.07\left(\frac{T_{\mathrm{cmb}}-3000}{500}\right) - 4.416\left(\frac{n_{\mathrm{craton}}}{3} - 1\right)$	
	$-$	$0.893\left(\frac{H}{2.72\cdot10^{-12}} - 1\right) - 1.043\left(\frac{1.57\cdot10^{22}}{\eta_0} - 1\right)$	7.31 (K)
Compressible convection-melting-whole mantle			Stand. Dev.
$\ln\left(\mathrm{corr}_{i,\mathrm{C,T}} - 1.148\right)$	$=$	$0.980 - 3.154\left(\frac{\mathrm{degree}}{3} - 1\right)$	6.77 (K)
Compressible convection-melting-upper part of mantle			Stand. Dev.
$\ln\left(\mathrm{corr}_{i,\mathrm{C,T}} + 6.254\right)$	$=$	$2.711 - 0.810\left(\frac{\mathrm{degree}}{3} - 1\right) - 0.733\left(\frac{T_{\mathrm{cmb}}-4000}{500}\right)$	4.98 (K)
Incompressible convection-no melting			Stand. Dev.
$\langle\frac{\mathrm{corr}_{\mathrm{C,T}}}{\partial t}\rangle$	$=$	$61.97 + 22.81\left(\log\left(\frac{1.57\cdot10^{22}}{\eta_0}\right) - 1\right) + 2.56\left(\frac{n_{\mathrm{craton}}}{3} - 1\right)$	
	$+$	$13.2\left(\frac{T_{\mathrm{cmb}}-3000}{500}\right) + 7.61\left(\frac{H}{2.72\cdot10^{-12}} - 1\right)$	7.31 (K/Gyr)
Compressible convection-melting-whole mantle			Stand. Dev.
$\langle\frac{\mathrm{corr}_{\mathrm{C,T}}}{\partial t}\rangle$	$=$	$61.34 + 9.05\left(\frac{T_{\mathrm{cmb}}-4000}{500}\right) - 26.29\left(\frac{T_{\mathrm{cmb}}-4000}{500}\right)^2$	1.83 (K/Gyr)
Compressible convection-melting-upper part of mantle			Stand. Dev.
$\langle\frac{\mathrm{corr}_{\mathrm{C,T}}}{\partial t}\rangle$	$=$	$87.95 + 12.03\left(\frac{T_{\mathrm{cmb}}-4000}{500}\right) - 7.08\left(\frac{T_{\mathrm{cmb}}-4000}{500}\right)^2$	
	$-$	$20.71\left(n_{\mathrm{craton}} - 1\right)$	5.30 (K/Gyr)

Note. $\mathrm{corr}_{i,\mathrm{C,T}}$ is the correlation amplitude of the degree that shows the highest value. These simple estimations are designed to show the relative importance of different parameters but are not based on a physical model. They should therefore not be physically interpreted or extrapolated.

or an increase of internal heating rate both tend to decrease the magnitude of the correlation between continents and subcontinental mantle temperature. In both cases, convective stirring laterally scatters thermal anomalies, which intrinsically decreases the correlation. This naturally happens when the reference viscosity is low as the flow is vigorous and small wavelengths form while broader plumes are no longer present. When strong radiogenic heating is considered, strong stirring takes some time to appear as it arises from the decrease of viscosity with time.

3.1.3. Effect of the Core Temperature

Cases with $T_{\mathrm{cmb}} = 2000$ K (for example, see Figures A1s1 and A2s1) show similar processes of rising mantle plumes, subduction, and entrainment of cold slabs in the convecting mantle and a buildup of elevated temperatures in the subcontinental mantle. Yet the low core temperature does not allow the mantle to maintain an internal temperature, which is comparable to the observed present-day value. Large downwellings strongly decrease the ambient temperature well below 1000 K, which leads to an unrealistic situation where the mantle has huge blobs of high viscosity and the entire lithosphere starts to drift. We do not use these cases for our empirical regressions of correlation amplitude (discussed further in section 4.4.1). In cases with $T_{\mathrm{cmb}} = 4000$ K (for example, see Figures 2e and 3e), there are many more thermal instabilities at the bottom, which is expected with a hotter core. Again, the region of subcontinental mantle warming develops (seen as degree-1 correlation in Figure 3e) but this warm thermal anomaly disappears over time due to a stronger convective flow.

3.1.4. Evolution of Surface and CMB Heat Flows

Figure 4 represents the evolution of the heat flow of the simulations previously discussed (Figures 2 and 3). We display surface and CMB heat flows see purple and green curves with left y axis. The normalized difference between top and bottom heat flows is also shown (see yellow curve with right y axis). This quantity reflects the evolution of average temperature of the mantle in cases without internal heating and converges to 0 when the equilibrium is reached. When internal heating is active, the heat flow difference also reflects the amount of radiogenic heating, preventing it from reaching 0 even if an equilibrium is found (as seen in Figure 4d).

Figures 4a–4c shows that the simulations excluding internal heating and considering a realistic core temperature (3000 K in incompressible convection simulations correspond to ~4000 K in reality when considering the adiabatic temperature increase with depth) quickly reach an equilibrium. The heat flows themselves stabilize, and their time-averaged difference is close to 0, with significant short time scale fluctuations. A slight tendency for cooling is more visible in case c, which has two continents initialized at non-antipodal positions. Figure 4d shows that radiogenic heating warms up the planet. The last two billion years of evolution show the equilibrium state in which radiogenic heating stabilizes the difference between surface and CMB heat flows. One can see that the initial difference between the heat flows is lower, which means that the mantle is warming up (also seen in Figure 2d). Figure 4e shows that the planet gradually warms up due to the large core temperature. The average heat flow difference is slightly negative, and the absolute values of heat flows slightly increase with time. This is due to the decrease in internal viscosity of the mantle. However, the heat flows do not vary more than ~10%.

Although Figure 4 depicts the general thermal evolution of the planet, we do not find a direct correlation between heat flows (or their difference) and the evolution of the continent-temperature correlation.

3.2. Second Set of Simulations: Compressible Convection With MCP

In this second set of simulations, we used a more realistic setup in which the core cools with time, and more importantly, melting and crustal production are considered. As these features result in much higher computational costs, a smaller number of simulations were run in the selected parameter space.

The primary distinguishing aspect of these models is the inclusion of melting of pyrolytic mantle and the subsequent basaltic crustal production. Two different correlation windows w_T define the depth range over which the temperature field is averaged with $w_{T1} = 300–2,890$ km and $w_{T2} = 300–1,000$ km. Continental thickness is initialized as 230 km, and all the cases have basal heating with a reference viscosity $\eta_0 = 10^{20}$ Pa·s (the viscosity now also depends on pressure). The initial potential temperature is 1900 K in this set of simulations. For numerical reasons, there is no radiogenic heating in these simulations. Unlike the incompressible convection cases, no thermal anomaly is introduced in the models because it might lead to an artificial melting event.

3.2.1. Qualitative Observations

In this set of simulations, the mechanical behavior leading to cooling around the continents by the formation of downwellings at the continental margins is also observed, but the melting and crustal production events break the continents apart and therefore destroy the correlation.

Figure 5a shows the time dependence of the correlation for harmonic degrees 1–10, while the breakup of a supercontinent is illustrated in Figure 5b on global (annuli) and local (white boxes) scales with a further magnification of the key regions (yellow boxes) for case g (given in Table 5). A degree-1 correlation with an amplitude ~30 K can be seen in Figure 5a, indicating that the subcontinental mantle is hotter than the suboceanic mantle. A spike in this correlation amplitude (up to 67 K) at time $t_1 = 713$ Myr is observed when a mantle plume reaches the upper mantle and results in voluminous magmatism. Following this, the correlation in higher degrees albeit with lower amplitudes is observed owing to supercontinent breakup. A quick comparison between the initial state and the later stages of the simulation shows that the continental material gets deformed and thinned over time owing to convective stresses.

At time $t_1 = 713$ Myr in Figure 5b, the elevated subcontinental temperatures and the arrival of a mantle plume in the subcontinental region cause temperatures that exceed the pyrolytic mantle solidus. This results in decompression melting of the hot asthenospheric mantle (White & McKenzie, 1989), which generates basaltic melt (light blue). If this melt is in the top 300 km, then it is instantaneously removed from this depth and placed at the surface above the continents to create oceanic crust or continental flood basalt (pink, ≥30% in a cell) and simulate volcanic eruption (see section 2.4 for implementation details). With time, this basaltic material gets buried and transforms into eclogite at a depth of 60 km following the phase changes introduced in section 2.3. Eclogite is around 190 kg/m^3 denser than olivine, and its negative buoyancy creates stresses that weaken the continents. This cold eclogitic crust along with the continental material becomes gravitationally unstable in the lithosphere (Lourenço et al., 2016) and starts to sink into the lower mantle. As a result of this downgoing material, a return flow develops in the mantle. A combination of this dense eclogitic material and the return mantle flow thins the continent inducing a continental rift at time $t_2 = 782$ Myr. By time $t_3 = 785$ Myr, the supercontinent breaks apart into two smaller continents, which start to drift in opposite directions. Following the breakup, small-scale sublithospheric convection (Ballmer et al.,

10.1029/2018GC007586

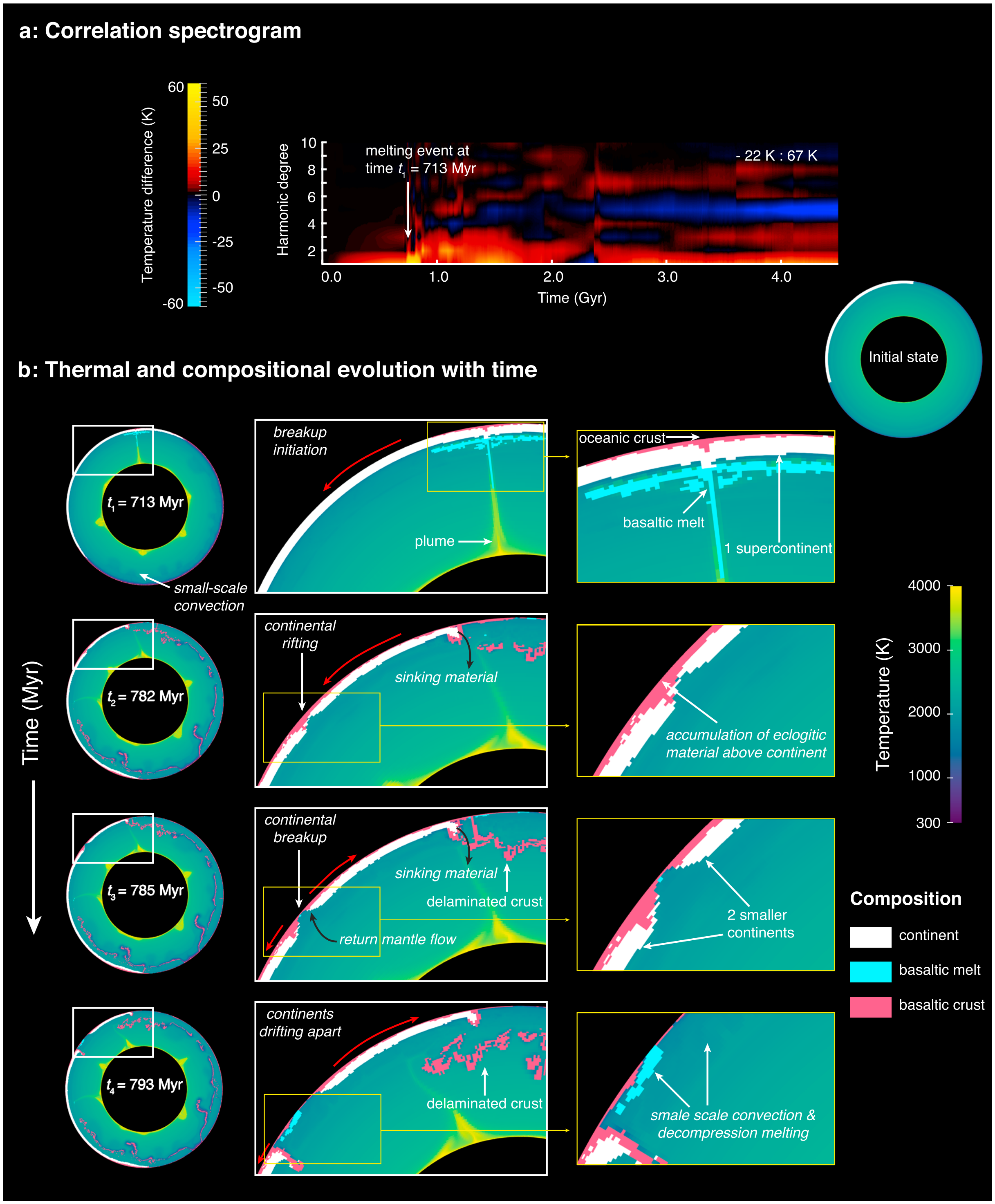

Figure 5. Continental breakup in a compressible convection simulation (case g) with melting-induced crustal production, 4000 K core-mantle boundary temperature, supercontinent, no internal heating, and correlation temperature window w_{T2}. (a) Spectrogram showing how the dominant harmonic degree changes with time. (b) Thermal and compositional evolution with time on global (annuli) and local (white boxes) scales with a further magnification of the key regions (yellow boxes). Superimposed over the temperature field are the continents (white), basaltic melt (light blue), and basaltic crust (pink, ≥30% in a cell). Red arrows indicate the direction of continental drift. Also shown is the initial state of the simulation.

10.1029/2018GC007586

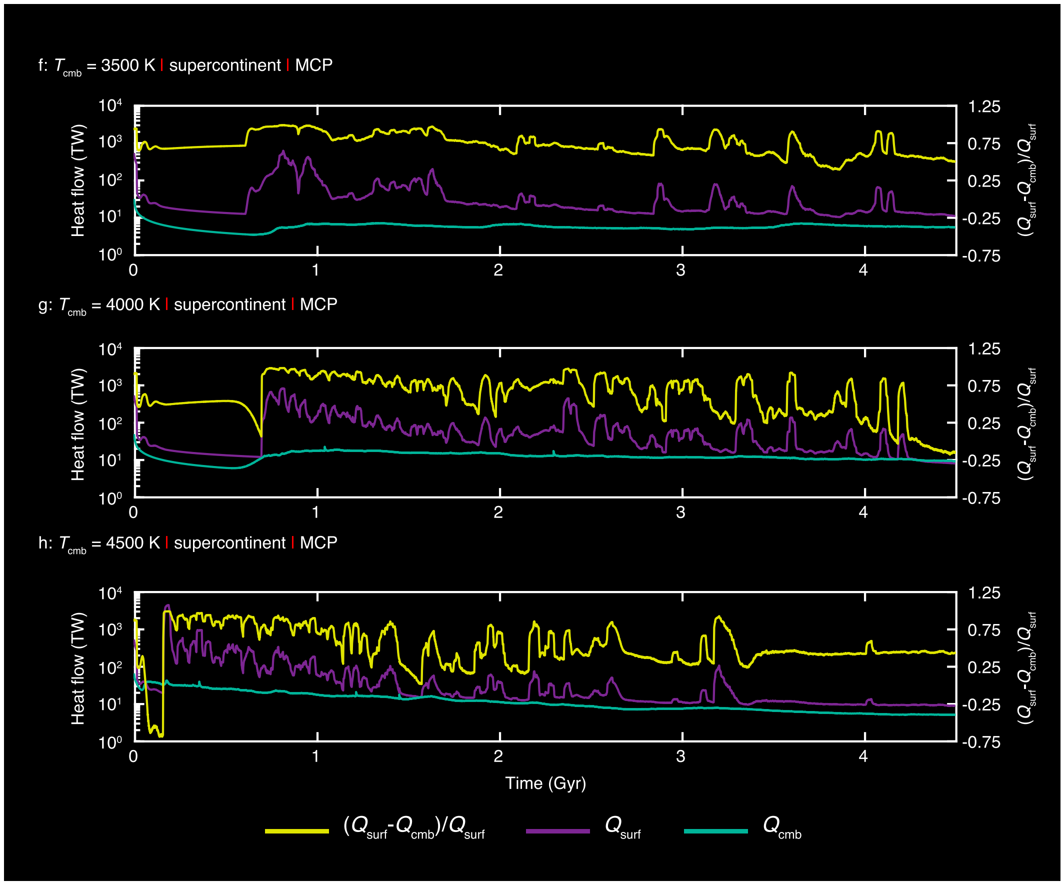

Figure 6. Time series of heat flow at the core-mantle boundary Q_{cmb} and at the surface Q_{surf} on the left y axis for the cases f–h featuring compressibility and melting-induced crustal production. Also shown on the right axis is the fraction of internal heating $(Q_{surf} - Q_{cmb})/Q_{surf}$ as a function of time. The thermal and compositional evolution along with the correlation spectrogram of case g is depicted in Figure 5.

2007; Bonatti & Harrison, 1976; Buck & Parmentier, 1986; Haxby & Weissel, 1986; Marquart et al., 1999) starts in the subcontinental mantle at time $t_4 = 793$ Myr causing further decompression melting and the continent-temperature correlation fades away. The buildup of a new correlation requires large-scale mantle flow reorganization, which might never happen if the continents are too small or too mobile.

As the thermal boundary layer grows faster in the suboceanic mantle, small-scale sublithospheric convection cells develop there earlier than time $t_1 = 713$ Myr. As a result of partial melting in the suboceanic mantle, latent heat is consumed and this also contributes toward the aforementioned correlation. Supercontinent breakup happens over a period of ∼70 Myr in the model presented here. The timing of this breakup might strongly depend on the reference viscosity, which was not tested in this set of simulations. In simulations with lower initial core temperature of 3500 K, similar continental breakup can last up to 300 Myr.

3.2.2. Evolution of Surface and CMB Heat Flows

Figure 6 shows the evolution of heat flow for three cases f–h (given in Table 5) each with a supercontinent but with a different initial core temperature. As core cooling is considered in simulations featuring compressible convection, a decrease in the CMB heat flow Q_{cmb} is observed throughout their evolution. The positive fluctuations in the Q_{surf} are attributed to the arrival of successive mantle plumes, which cause decompression melting. These fluctuations become more frequent for cases with higher initial core temperature as they have a larger number of thermal instabilities at the bottom boundary. The initial spikes in the Q_{surf} are because of the large amount of heat being transferred to the surface with the eruption of basaltic melt. An equilibrium regime is never reached in these simulations as the core never stops cooling. All simulations stopped with a CMB heat flow between 5 and 10 TW.

4. Discussion

4.1. Empirical Regressions of the Continent-Temperature Correlation

Our spectral decomposition of temperature and composition fields allows us to quantify the correlation between continents and subcontinental mantle temperature (and negative temperature anomalies away from continents). Using most of the cases listed in Table 4 (see superscripts in the table for details), we were able to find a first-order empirical equation to quantify the magnitude of the correlation. Table 6 summarizes our estimations for the first and second sets of simulations. For the first set of simulations, four parameters have been used to perform the regression of the correlation: T_{cmb}, n_{craton}, H, and η_0. For the second set, H and η_0 were identical in all simulations and are therefore absent from the regressions. Two fits are provided for the second set of simulations as we perform correlations in the entire mantle (300–2,890 km) and upper part of mantle (300–1,000 km).

Estimating the relative impact of our input parameters on the intensity of the continent-temperature correlation is a difficult exercise as there is no physical model providing an analytical expression. Moreover, the correlation sometimes takes negative values, which makes it impossible to employ standard power law formulations as is commonly done in boundary layer theory for various quantities. We have tried various expressions to attempt to best fit the correlation: linear functions, power law, exponential, linear times exponential, hyperbolic tangent, and so forth. In all cases, many parameter combinations were tested. It appears that the regression giving the lowest standard deviation (within this small space of functions listed above) is achieved by adding a constant to the correlation to make it always positive and then taking the logarithm of the sum, as shown in Table 6. This arbitrary logarithmic expression reflects the small influence of most parameters when the correlation is low. In our tests, using a power law expression of the sum of the correlation with a constant gave a very similar standard deviation and showed identical relative importance of the parameters. We emphasize that the reader should not attempt to extrapolate these regressions away from the parameter window of the current study as they are not obtained from a physics-based scaling law.

Using our physically arbitrary formulation, we observe that an increase in T_{cmb}, n_{craton}, and H or a decrease in viscosity, all lead to a decrease in correlation. The dominant degree was used to fit the second set of simulations instead of the initial number of continents as the continents are split in several parts and therefore their number varies. Looking at the entire mantle, we find that the core temperature plays a negligible role in forming a correlation. Yet the third row in Table 6 shows that the correlation between the temperature of the upper part of the mantle and the continents strongly depends on the core temperature. This shows that the plumes provide large temperature anomalies in the upper part of the mantle but contribute less to the formation of low-degree patterns in the lower mantle. Moreover, broad downwellings tend to gather in the lower mantle disregarding the continental configuration at the surface due to the spherical geometry.

Figure 7a plots the correlations used to perform the empirical fits (on the y axis) versus the results of the fits (x axis). Globally, correlation amplitudes are between 0 and 40 K but also reach up to 100 to 200 K. Amplitudes of correlations in simulations considering melting and crustal production reach a maximum of 30 to 60 K (red squares and purple diamonds, respectively). Overall, regressions are of good quality as the standard deviations are of the order of 5–7 K (see Table 6).

4.2. Empirical Regressions of the Evolution of the Continent-Temperature Correlation

The last columns of Tables 4 and 5 show the average evolution of the continent-temperature correlation. In Table 6 and Figure 7b, we present empirical regressions of this evolution.

Concerning the spectral analysis of the evolution of continent-temperature correlation, two important points should be noted. First, $< \partial \mathrm{corr}/\partial t >$ (see equation (15)) is not directly equal to the increase of absolute temperature below continents as it also reflects the decrease of temperature due to downwellings around the continents. Second, $< \partial \mathrm{corr}/\partial t >$ provides an average of the independent evolution of several harmonics (up to degree-6 in the present study). In real space, harmonics might locally sum up and provide a much larger or much lower correlation increase. Yet the rather low standard deviations presented in Table 6 show that insightful trends and orders of magnitude can be obtained using this method.

Overall, it appears that the evolution of the continent-temperature correlation is on the order of 10–100 K per billion year (see Tables 4 and 5 and Figure 7b). In our cases featuring incompressible convection, we observe that decreasing the reference viscosity or increasing the number of continents, the initial core temperature

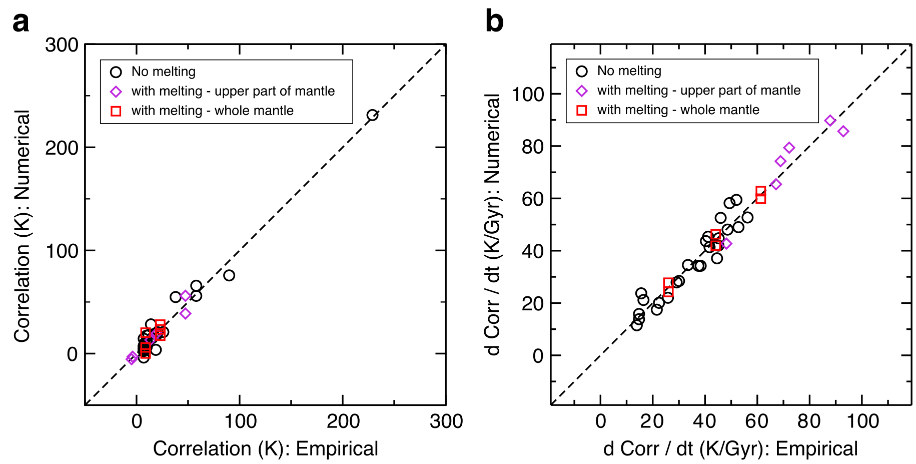

Figure 7. (a) Numerical continent-temperature correlations (K) (y axis) versus their empirical regressions as defined in Table 6 (x axis) for all cases. (b) The evolution of the correlation with time (see equation (15)). Black circles represent the first set of simulations with no melting and crustal production; diamonds and squares depict the results of the second set of simulations. Correlations are of the order of tens to hundreds of kelvins.

or the internal heating results in an increase in the time dependence of the correlation (see the fourth row in Table 6). Each of these contributions is discussed further.

A low viscosity favors both convective cooling around the cratons and their mobility. When the viscosity is low, downwellings can quickly cool a large volume of mantle surrounding the regions below the cratons, resulting in a rapid growth of correlation with time. Moreover, when cratons drift above cold regions, the continent-temperature correlation also quickly drops. The kinetics of both processes are increased by lower viscosities.

Increasing the number of continents slightly increases the time dependence of the correlation. Although this effect is minor, it might be due to the fact that numerous continents are smaller in size, which makes it more difficult to maintain a potential correlation. A large core temperature generates warm plumes, which slow down mantle cooling, tend to increase subcontinental mantle temperatures, and push continents laterally. These three mechanisms lead to a larger time dependence of the correlation. Finally, internal heating tends to both increase the subcontinental mantle temperature and decrease the ambient viscosity. Both mechanisms lead to a high time dependence of the correlation.

In compressible convection cases, looking at the entire mantle (fifth row in Table 6), we observe that the time dependence of the correlation is maximal for a core temperature of 4000 K (and not 4500 K as could be expected). We chose to represent this nonlinearity by a second-order polynomial in our regressions (see Table 6, fifth and sixth rows). This can be explained by the fact that the lowest core temperature considered here (3500 K, for example, in case f) does not generate very vigorous plumes. The mantle therefore cools more efficiently, which increases the viscosity and slows down the kinetics of convection. On the contrary, a large core temperature (4500 K, for example, in case h) generates such widespread magmatism that continents are rapidly destroyed. Moreover, lateral motion of the continent is observed in the simulation employing a core temperature of 4000 K (case g). This is due to the fact that enough crust is produced to create strong lateral density gradients in the lithosphere, leading to the mobility of the continent. When looking at the upper part of the mantle in compressible convection cases (sixth row in Table 6), one can see that the time dependence of the correlation always increases with increasing core temperature, although we still observe some nonlinearity as shown by the second-order term. Overall, both the magnitude of the correlation and its time dependence are higher when looking at the upper part of the mantle.

4.3. Illustration of our Regressions

Figure 8 illustrates the regressions for continent-temperature correlation in the upper part of the mantle as presented in Table 6. Since we did not systematically vary internal heating and the reference viscosity in our compressible convection models, we inferred the influence of these parameters as determined from regressions for incompressible convection cases to estimate their influence on the correlation. We obtained a composite formulation based on both compressible and incompressible convection simulations, which

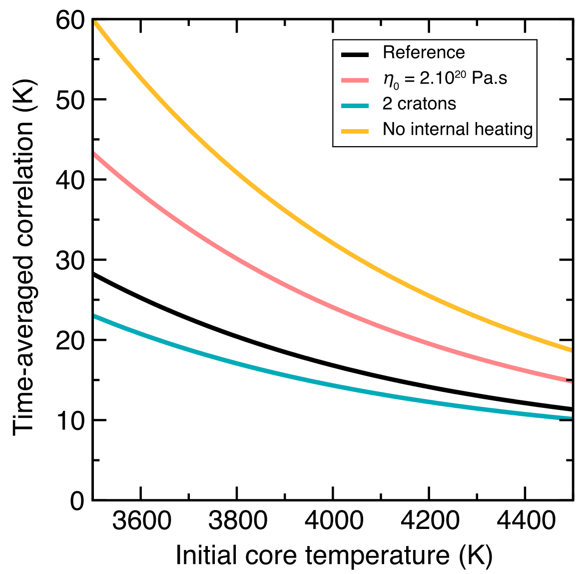

Figure 8. Illustration of the empirical regressions: continent-temperature correlations as a function of initial core temperature. The set of parameters representing the reference case is $\eta_0 = 10^{20}$ Pa·s, $H = 3 \cdot 10^{-12}$ W/kg, one craton, and $T_{\text{cmb}} = 4000$ K.

contains the four contributions of internal heating, reference viscosity, number of continents, and initial core temperature. We obtained the following equations:

$$\begin{aligned}\text{corr} = 6.254 + \exp\Bigg[& 2.711 - 0.733\left(\frac{T_{\text{cmb}} - 4000}{500}\right) - 0.81\left(\frac{n_{\text{craton}}}{3} - 1\right) \\ & - 0.893\left(\frac{H}{2.72 \cdot 10^{-12}}\right) - 1.043\left(\log\left(\frac{10^{21}}{\eta_0}\right) - 1\right)\Bigg]\end{aligned} \tag{16}$$

$$\begin{aligned}\left\langle \frac{\text{corr}_{\text{C,T}}}{\partial t} \right\rangle = {} & 87.95 + 12.03\left(\frac{T_{\text{cmb}} - 4000}{500}\right) - 7.08\left(\frac{T_{\text{cmb}} - 4000}{500}\right)^2 \\ & - 20.71\left(n_{\text{craton}} - 1\right) + 22.81\left(\ln\left(\frac{10^{21}}{\eta_0}\right) - 1\right) \\ & + 7.61\left(\frac{H}{2.72 \cdot 10^{-12}}\right)\end{aligned} \tag{17}$$

Figure 8 represents the correlations obtained using our regression (equation (16)). The impact of initial core temperature on the correlation is represented for an Earth-like range. Initial core temperature in the Archean Earth was most probably higher than the present-day value, which is considered to be close to 4000 K. We show how the correlation decreases with core temperature. Figure 8 also shows that increasing the viscosity by a factor 2 adds 5–15 K to the temperature anomalies below continents. Suppressing internal heating increases the correlation by 10–30 K. Considering two cratons instead of one supercontinent only decreases the temperature anomalies by few kelvins. Again, one should keep in mind that these absolute values are an average of the low degrees, which are potentially locally additive.

Equation (17) shows that a large core temperature tends to make the correlation very time dependent. On the contrary, a low core temperature generates larger correlations subject to slower evolutions. Increasing the viscosity by a factor 2 or removing internal heating slows down the oscillations by a factor 2 for the reference case represented in Figure 8. Finally, considering two cratons instead of one tends to slightly slow down the evolution although it decreases the correlation itself.

4.4. Implications of Our Results

Even though our global models are rather simplified when compared to the real Earth, they help us understand and make general remarks on the long-term thermal and mechanical influence of continents on the underlying mantle and vice versa. In this section, we illustrate the significance of our results and support them by comparing them to geological and geophysical observations as well as previous numerical studies.

4.4.1. Previous Work, Model Parameters, and Seismic Observations

Our models show that continents are capable of trapping heat in the underlying mantle causing subcontinental mantle warming. The amplitude of this warming changes with continental extent, CMB temperature, reference viscosity, and internal heating. A higher amplitude is observed with a supercontinent (up to 237 K, see Figure 3a), and it decreases with smaller extent of the continents. This finding agrees with the previous results of Coltice et al. (2007), Lenardic et al. (2011), O'Neill et al. (2009), Phillips and Coltice (2010), and Rolf et al. (2012), all of whom reported elevated temperatures below continents in their numerical studies. Furthermore, our models show that such thermal anomalies in the subcontinental mantle can persist for hundreds of millions of years and even when the continents are mobile. In all our models, the development of subduction zones along continental margins helps in enhancing the thermal contrast between subcontinental and suboceanic mantle. Similar behavior has been observed in the prior work of Heron and Lowman (2011), Heron et al. (2015), Lenardic et al. (2011), and O'Neill et al. (2009).

We have tested the impact of basal heating on correlation by initializing our models with different CMB temperature at the bottom boundary. The need to test this arises due to the uncertain nature and contribution of CMB heat flow toward mantle dynamics. Continental motion is attributed to the viscous stresses imparted by the convecting mantle, and the extent of this motion depends on the heat budget of the mantle. CMB heat flow, internal heating from decay of radioactive elements in the mantle, and secular mantle cooling contribute to this heat budget. Recent indications that the core's thermal conductivity may be 3 times higher than previously inferred mineral physics estimates (de Koker et al., 2012; Gomi et al., 2013; Pozzo et al., 2013), and the inclusion of the post-perovskite phase change in the lower mantle (Hernlund et al., 2005) constrain the heat flow from the core to be in the range of 10–16 TW (Lay et al., 2006, 2008; Hernlund, 2010; van der Hilst et al., 2007; although a lower core thermal conductivity has been advocated by Zhang et al., 2015). Some mantle convection models (Leng & Zhong, 2008; Mittelstaedt & Tackley, 2006; Zhong, 2006) have shown that plume heat flux can account for a significant fraction of the CMB heat flux and plume heat flux decreases by as much as a factor of 3 as the plumes ascend to the upper mantle, implying that mantle plumes should be considered when studying mantle dynamics coupled with continents.

Table 4 gives the CMB heat flow and v_{RMS} of the whole mantle for all the cases featuring incompressible convection averaged over their simulation time. Cases with $T_{\mathrm{cmb}} = 3000$ K give CMB heat flow and v_{RMS} of the order of 11–13 TW and 0.25–0.45 cm/year, respectively. The heat flow values obtained from these models are in agreement with the recent heat flow estimates as discussed above and the low RMS velocity of the whole mantle can be attributed to the lack of internal heating. Our models without internal heating show a general trend of decreasing correlation with increasing T_{cmb}. Comparing the CMB heat flow from these models with the recent heat flow estimates, we argue that CMB temperatures of 2000 or 4000 K are not realistic values in an incompressible convection setup. Moreover, it should be noted that in an incompressible convection model with $T_{\mathrm{surf}} = 300$ K and $T_{\mathrm{cmb}} = 3000$ K, the entire 2700 K superadiabatic temperature difference will drive convection whereas in a compressible convection model, around 1000–1200 K of the difference between the CMB and surface temperatures will be taken up by an adiabatic temperature increase and only the remaining 1500–1700 K will drive convection. This implies that a given T_{cmb} in an incompressible convection model will give similar behavior (e.g., in terms of plumes excess temperature) to one about 1000–1200 K higher in a compressible convection model.

When included, internal heating increases the effective convective vigor of the mantle and makes for a drastic change in the style of mantle dynamics. The internal temperature is higher and a decrease in the number of slabs stagnating at the lower boundary is observed. The more effective mantle mixing lowers the thermal isolation between the subcontinental and the suboceanic mantle. Compared to the models with only basal heating, the amplitude of degree-1 decreases (Figures 3d and A2s3), and for cases with low reference viscosity, no correlation is observed. This is in agreement with the main findings of Heron and Lowman (2014) who also report a decreasing influence of continental insulation on subcontinental warming with increasing Ra.

Numerous seismic tomographic studies (e.g., Grand, 2002; Houser et al., 2008; Li & Romanowicz, 1996; Masters et al., 2000; Panning & Romanowicz, 2006; Ritsema et al., 1999, 2011; Su & Dziewonski, 1997; Su et al., 1994; van der Hilst et al., 1997; Zhao, 2004) have unanimously observed slow *S* wave velocity anomalies beneath present-day Africa and South Pacific, indicating a degree-2 structure for the Earth's mantle. Though our models only show a dominant degree-1 structure with a supercontinent (Figures 2a and 3a) and degree-2 with two continents (Figures 2b and 3b), these qualitative observations from our models might have been relevant in early geological history.

4.4.2. Continental Rifting and Flood Basalts

It has been suggested that mantle plumes can cause intense magmatic activity while emplacing CFB followed by continental rifting and fragmentation (Campbell & Griffiths, 1990; Condie, 2004; Morgan, 1972; Richards et al., 1989; Scrutton, 1973; White & McKenzie, 1989). Studies have also shown the propensity of plumes to rise and concentrate under the relatively hotter subcontinental mantle (e.g., Guillou & Jaupart, 1995; Gurnis, 1988; Lowman & Jarvis, 1993, 1996; Phillips & Bunge, 2005; Zhong & Gurnis, 1993).

Flood basalts are large accumulation of basaltic lava formed in a series of large eruptions lasting for about 1–10 Myr (Courtillot & Renne, 2003) and covering stretches of continents or oceanic floor. Prominent examples of CFB include the 65 Ma Deccan Traps in India that coincide with the opening of the NW Indian Ocean (Courtillot et al., 1986, 1988), the 200 Ma Central Atlantic Margin Province (CAMP) flood basalts that coincide with the opening of the Central Atlantic Ocean (Courtillot et al., 1999) and the 250 Ma Siberian Traps (Wooden et al., 1993). Examples of flood basalts that were emplaced without continental rifting are the Ontong Java Plateau (Neal et al., 1997) and Columbia River basalts (Hooper et al., 2007; Rampino & Stothers, 1988).

Anderson (1982) proposed that continental assembly would cause subcontinental mantle warming and the breakup of Pangea, thereby offering an alternative source of CFB. The purely internally heated models of Coltice et al. (2009, 2007) supported and quantified this proposal without the involvement of mantle plumes. They showed that continental aggregation induced elevated subcontinental mantle temperatures and large-scale melting events might have caused the emplacement of CAMP flood basalts following Pangea's breakup.

Our model featuring compressibility with melting and crustal production presented in Figure 5b favors the mantle plume origin for the origin of CFB. The plumes that rise up to the upper mantle result in voluminous magmatism, producing a basaltic crust. This basaltic material transforms into denser eclogite at a depth of 60 km and starts to sink into the mantle, generating a return mantle flow. The eclogitic crust combined with the return mantle flow induce continental rifting and breakup. This scenario represents a mix of both passive (lithospheric extension by plate forces) and active (mantle plume) rifting volcanism as proposed by Sengör and Burke (1978). These results are in contrast to the findings of O'Neill et al. (2009) who did not observe any voluminous volcanism and supercontinent breakup in their simulations. These voluminous basalt-generating events in our model can be likened to the emplacement of CAMP CFB following the breakup of Pangea. To summarize, MCP plays a vital role in the evolution of continent-temperature correlation in two different ways. It increases the correlation by consuming latent heat and effectively cooling the suboceanic mantle. It decreases the correlation as decompression melting underneath the continents result in voluminous magmatism, which is followed by continental rifting and breakup. Moreover, the development of small-scale sublithospheric convection cells reduces the thermal contrast between the subcontinental and suboceanic mantle, which is in alignment with the findings of O'Neill et al. (2009).

Geological evidence also points toward the eruption of ultramafic mantle-derived volcanic rocks such as komatiites (Nisbet, 1982) above Archean greenstone belts (primordial continents), for example, in the Yilgarn craton of Western Australia (Mole et al., 2014; Wang et al., 1996) and the Dharwar craton of Southern India (Jayananda et al., 2008). Our models with MCP can also be applied to such scenarios.

In the past, many studies of models featuring varying complexity have tried to answer the question of whether continents warm up the subcontinental mantle. We contribute to this discussion by offering qualitative observations from 2-D mantle convection simulations with mobile continents. Furthermore, we provide numbers quantifying the magnitude of this continent-temperature correlation and its time dependence by employing simple empirical regressions. Starting with simple incompressible convection models, we show that the dominant degree of correlation changes with continental distribution and subcontinental temperature amplitude can reach up to 200 K, depending on the extent of the continents. It should be noted that this result was obtained over long time scales and with a convective vigor much less compared to the real Earth. We also show that this correlation decreases with increasing core temperature, number of continents, radiogenic heat production, or decreasing reference viscosity. These results reaffirm the previous findings of Heron and Lowman (2014), Lenardic et al. (2011), O'Neill et al. (2009), Phillips and Coltice (2010), and Rolf et al. (2012). When using a more realistic setup with compressible convection, core cooling, and MCP,

10.1029/2018GC007586

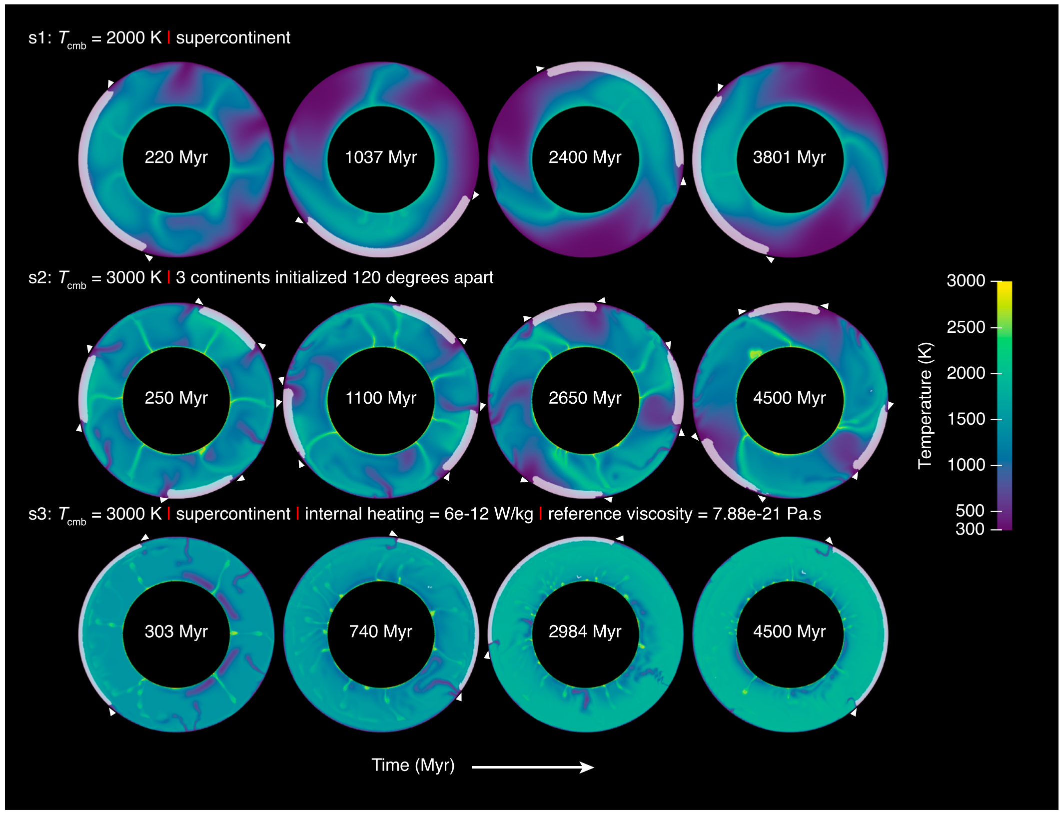

Figure A1. Thermal evolution of the additional cases s1–s3 featuring incompressibility and without melting-induced crustal production. White triangles demarcate the continents, which are represented by composition field (white) superimposed over the temperature field. A small thermal anomaly of 125 K is introduced in the mid-mantle at 3 o'clock in all these models.

our models demonstrate the impact of magmatism on the dynamics of continents. We observe that decompression melting in the mantle as a result of a mantle plume or small-scale sublithospheric convection leads to voluminous volcanism. The emplacement of dense-eclogite material at the surface breaks the continents apart and drastically reduces this correlation (amplitude of tens of kelvins).

These models have, however, some limitations, which should be addressed in future studies. Continents do not break in our incompressible convection models because they have a higher yield stress and higher viscosity than noncontinental material. Accordingly, the reader should not make inferences about the timings and the related effects of supercontinent assembly or breakup from these models. When supercontinents do rift owing to magmatism in compressible convection simulations with MCP, the duration of this rifting depends on the initial core temperature. If these models were migrated to three dimensions, then the expected diminished effects of plumes in the upper mantle and subducting slabs in the lower mantle would likely result in more homogenous mantle temperature profiles and lower correlation amplitudes. Further modeling efforts should also include real continental growth by differentiation of the mantle, instead of using prescribed continents. In this study, we considered fully eruptive magmatism. In the future, the influence of plutonism on this correlation should be explored as it has been to shown to play an important role in shaping the Earth's lithosphere (Crisp, 1984; Cawood et al., 2013; Rozel et al., 2017).

5. Conclusions

We present new tools to quantify the time-dependent correlation between continents and the underlying mantle, then use them to advance our understanding of the magnitude and causes of this correlation and its time dependence, compared to the more qualitative findings of previous modeling studies.

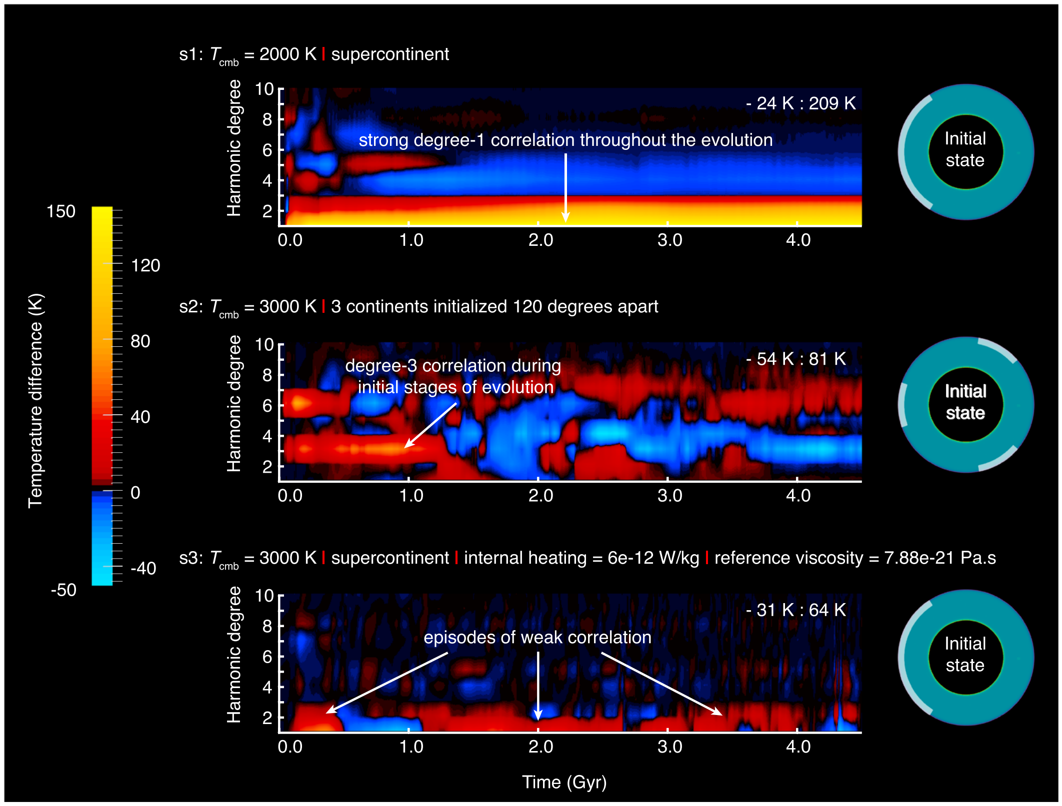

Figure A2. (left) Spectrogram of the additional cases s1–s3 featuring incompressibility and without melting-induced crustal production, where positive (red to yellow) and negative (shades of blue) values indicate correlation and anticorrelation between continental material at the surface and elevated temperatures underneath, respectively (using temperature correlation window w_{T1}). Also shown are the minimum and maximum temperature contrasts obtained from the models. (right) Initial state of the models with continents (white).

We first apply them to incompressible models with a complexity very similar to that considered in the large body of published literature on the influence of continents on mantle convection. We demonstrate that the correlation between continents and the underlying mantle is systematic, predictable, and quantifiable using the tools presented in this study. Furthermore, we show that an analytical fit to both the time-averaged value and the time rate of change of this correlation is possible and give the mathematical form and best fitting coefficients. The correlation between continents and the underlying mantle is almost always positive, with a magnitude that decreases with increasing core temperature, number of continents, radiogenic heat production, and decreasing reference viscosity. The time rate of change of the correlation increases with increasing number of continents, initial core temperature or internal heating rate, or decreasing reference viscosity.

With the aid of heat flow time series, we show that the incompressible convection models rapidly reach statistically steady state and therefore the long-term statistical behavior is not influenced by the initial conditions.

We then apply the tools to a model setup more realistic than previously used in any studies of mantle convection with continents, one that incorporates compressibility, MCP, and core cooling. The above conclusions about correlations still apply to these models but they produce correlations that are much smaller in amplitude than the simpler, incompressible setup, a finding that points the way toward needed future research. These compressible convection models also exhibit continental rifting and breakup, thereby supporting the mantle plume origin of CFB.

Appendix A: Additional Figures

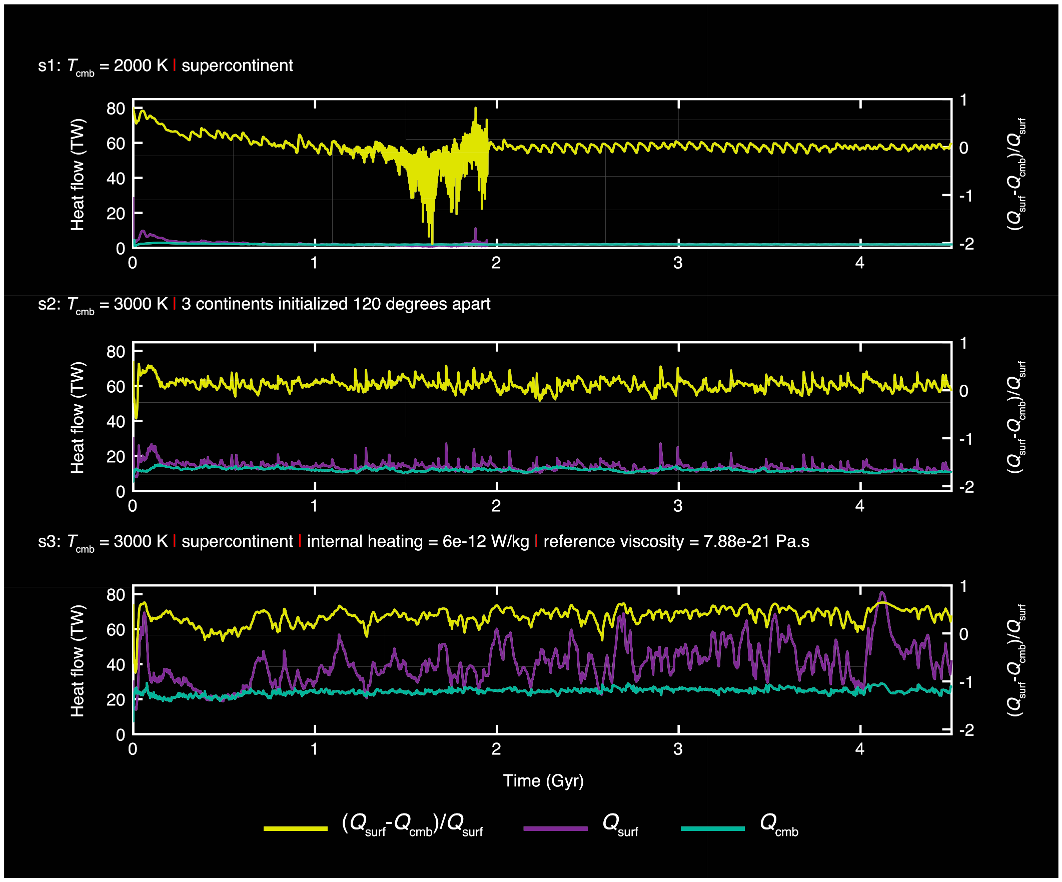

Figure A3. Time series of heat flow at the core-mantle boundary Q_{cmb} and at the surface Q_{surf} on the left y axis for the additional cases s1–s3 featuring incompressibility and without melting-induced crustal production. Also shown, on the right axis is the fraction of internal heating $(Q_{surf} - Q_{cmb})/Q_{surf}$ as a function of time.

Acknowledgments
We thank Adrian Lenardic, Allen McNamara, and two anonymous reviewers for their constructive reviews that helped improve the manuscript, and Thorsten Becker for his editorial work. C. Jain and A. B. Rozel received funding from the European Research Council under the European Union's Seventh Framework Programme (FP/2007-2013)/ERC Grant Agreement 320639 project iGEO. The raw data from the calculations, which are visualized and analyzed in this manuscript appear in the tables found in the supporting information. Further detail is available by contacting the corresponding author.

References

Amestoy, P. R., Duff, I. S., & L'Excellent, J. Y. (2000). Multifrontal parallel distributed symmetric and unsymmetric solvers. *Computer Methods in Applied Mechanics and Engineering*, *184*(2-4), 501–520.

Ammann, M. W., Brodholt, J. P., Wookey, J., & Dobson, D. P. (2010). First-principles constraints on diffusion in lower-mantle minerals and a weak D" layer. *Nature*, *465*(7297), 462–465.

Anderson, D. L. (1982). Hotspots, polar wander, Mesozoic convection and the geoid. *Nature*, *297*(5865), 391–393.

Ballmer, M. D., van Hunen, J., Ito, G., Tackley, P. J., & Bianco, T. A. (2007). Non-hotspot volcano chains originating from small-scale sublithospheric convection. *Geophysical Research Letters*, *34*, L23310. https://doi.org/10.1029/2007GL031636

Bonatti, E., & Harrison, C. G. A. (1976). Hot lines in the Earth's mantle. *Nature*, *263*(5576), 402–404.

Boyd, F. R. (1987). High-and low-temperature garnet peridotite xenoliths and their possible relation to the lithosphere-asthenosphere boundary beneath Africa. In P. H. Nixon (Ed.), *Mantle xenolith* (pp. 403–412). New York: John Wiley.

Boyd, F. R. (1989). Compositional distinction between oceanic and cratonic lithosphere. *Earth and Planetary Science Letters*, *96*(1-2), 15–26.

Buck, W. R., & Parmentier, E. M. (1986). Convection beneath young oceanic lithosphere: Implications for thermal structure and gravity. *Journal of Geophysical Research*, *91*(B2), 1961–1974.

Buffett, B. A., Huppert, H. E., Lister, J. R., & Woods, A. W. (1992). Analytical model for solidification of the Earth's core. *Nature*, *356*(6367), 329–331.

Buffett, B. A., Huppert, H. E., Lister, J. R., & Woods, A. W. (1996). On the thermal evolution of the Earth's core. *Journal of Geophysical Research*, *101*(B4), 7989–8006.

Campbell, I. H., & Griffiths, R. W. (1990). Implications of mantle plume structure for the evolution of flood basalts. *Earth and Planetary Science Letters*, *99*(1-2), 79–93.

Cawood, P. A., Hawkesworth, C. J., & Dhuime, B. (2013). The continental record and the generation of continental crust. *Geological Society of America Bulletin*, *125*(1-2), 14–32.

Chandrasekhar, S. (1961). *Hydrodynamic and hydromagnetic stability*. New York: Oxford University Press.

Christensen, U. R., & Hofmann, A. W. (1994). Segregation of subducted oceanic crust in the convecting mantle. *Journal of Geophysical Research*, *99*(B10), 19,867–19,884.

Čížková, H., van den Berg, A. P., Spakman, W., & Matyska, C. (2012). The viscosity of Earth's lower mantle inferred from sinking speed of subducted lithosphere. *Physics of the Earth and Planetary Interiors*, *200-201*, 56–62.

Coltice, N., Bertrand, H., Rey, P., Jourdan, F., Phillips, B. R., & Ricard, Y. (2009). Global warming of the mantle beneath continents back to the Archaean. *Gondwana Research*, *15*(3-4), 254–266.
Coltice, N., Phillips, B. R., Bertrand, H., Ricard, Y., & Rey, P. (2007). Global warming of the mantle at the origin of flood basalts over supercontinents. *Geology*, *35*(5), 391.
Coltice, N., Rolf, T., Tackley, P. J., & Labrosse, S. (2012). Dynamic causes of the relation between area and age of the ocean floor. *Science*, *336*(6079), 335–338.
Condie, K. C. (2004). Supercontinents and superplume events: Distinguishing signals in the geologic record. *Physics of the Earth and Planetary Interiors*, *146*(1-2), 319–332.
Cooper, C. M., Lenardic, A., & Moresi, L. (2006). Effects of continental insulation and the partitioning of heat producing elements on the Earth's heat loss. *Geophysical Research Letters*, *33*, L13313. https://doi.org/10.1029/2006GL026291
Cooper, C. M., Moresi, L. N., & Lenardic, A. (2013). Effects of continental configuration on mantle heat loss. *Geophysical Research Letters*, *40*, 2647–2651. https://doi.org/10.1002/grl.50547
Courtillot, V., Besse, J., Vandamme, D., Montigny, R., Jaeger, J. J., & Cappetta, H. (1986). Deccan flood basalts at the Cretaceous/Tertiary boundary? *Earth and Planetary Science Letters*, *80*(3-4), 361–374.
Courtillot, V., Féraud, G., Maluski, H., Vandamme, D., Moreau, M. G., & Besse, J. (1988). Deccan flood basalts and the Cretaceous/Tertiary boundary. *Nature*, *333*(6176), 843–846.
Courtillot, V., Jaupart, C., Manighetti, I., Tapponnier, P., & Besse, J. (1999). On causal links between flood basalts and continental breakup. *Earth and Planetary Science Letters*, *166*(3-4), 177–195.
Courtillot, V. E., & Renne, P. R. (2003). On the ages of flood basalt events. *Comptes Rendus Geoscience*, *335*(1), 113–140.
Crisp, J. A. (1984). Rates of magma emplacement and volcanic output. *Journal of Volcanology and Geothermal Research*, *20*(3-4), 177–211.
Davies, G. (2007). Thermal evolution of the mantle. In D. Stevenson & G. Schubert (Ed.), *Evolution of the Earth* (Vol. 9, pp. 197–216). New York: Elsevier.
de Koker, N., Steinle-Neumann, G., & Vlcek, V. (2012). Electrical resistivity and thermal conductivity of liquid Fe alloys at high P and T, and heat flux in Earth's core. *Proceedings of the National Academy of Sciences*, *109*(11), 4070–4073.
Gomi, H., Ohta, K., Hirose, K., Labrosse, S., Caracas, R., Verstraete, M. J., & Hernlund, J. W. (2013). The high conductivity of iron and thermal evolution of the Earth's core. *Physics of the Earth and Planetary Interiors*, *224*(C), 88–103.
Grand, S. P. (2002). Mantle shear-wave tomography and the fate of subducted slabs. *Philosophical Transactions of the Royal Society of London Series a-Mathematical Physical and Engineering Sciences*, *360*(1800), 2475–2491.
Grigné, C., Labrosse, S., & Tackley, P. J. (2007). Convection under a lid of finite conductivity in wide aspect ratio models: Effect of continents on the wavelength of mantle flow. *Journal of Geophysical Research*, *112*, B08403. https://doi.org/10.1029/2006JB004297
Guillou, L., & Jaupart, C. (1995). On the effect of continents on mantle convection. *Journal of Geophysical Research*, *100*(B12), 4217–24238.
Gurnis, M. (1988). Large-scale mantle convection and the aggregation and dispersal of supercontinents. *Nature*, *332*(6166), 695–699.
Hawkesworth, C. J., & Kemp, A. I. S. (2006). Evolution of the continental crust. *Nature*, *443*(7113), 811–817.
Haxby, W. F., & Weissel, J. K. (1986). Evidence for small-scale mantle convection from Seasat altimeter data. *Journal of Geophysical Research*, *91*(B3), 3507–3520.
Hernlund, J. W. (2010). On the interaction of the geotherm with a post-perovskite phase transition in the deep mantle. *Physics of the Earth and Planetary Interiors*, *180*(3-4), 222–234.
Hernlund, J. W., & Tackley, P. J. (2008). Modeling mantle convection in the spherical annulus. *Physics of the Earth and Planetary Interiors*, *171*(1-4), 48–54.
Hernlund, J. W., Thomas, C., & Tackley, P. J. (2005). A doubling of the post-perovskite phase boundary and structure of the Earth's lowermost mantle. *Nature*, *434*(7035), 882–886.
Heron, P. J., & Lowman, J. P. (2010). Thermal response of the mantle following the formation of a "super-plate". *Geophysical Research Letters*, *37*, L22302. https://doi.org/10.1029/2010GL045136
Heron, P. J., & Lowman, J. P. (2011). The effects of supercontinent size and thermal insulation on the formation of mantle plumes. *Tectonophysics*, *510*(1-2), 28–38.
Heron, P. J., & Lowman, J. P. (2014). The impact of Rayleigh number on assessing the significance of supercontinent insulation. *Journal of Geophysical Research: Solid Earth*, *119*, 711–733. https://doi.org/10.1002/2013JB010484
Heron, P. J., Lowman, J. P., & Stein, C. (2015). Influences on the positioning of mantle plumes following supercontinent formation. *Journal of Geophysical Research: Solid Earth*, *120*, 3628–3648. https://doi.org/10.1002/2014JB011727
Herzberg, C., Raterron, P., & Zhang, J. (2000). New experimental observations on the anhydrous solidus for peridotite KLB-1. *Geochemistry, Geophysics, Geosystems*, *1*(11), 1051–14.
Hirth, G., & Kohlstedt, D. L. (1996). Water in the oceanic upper mantle: Implications for rheology, melt extraction and the evolution of the lithosphere. *Earth and Planetary Science Letters*, *144*(1-2), 93–108.
Hooper, P. R., Camp, V. E., Reidel, S. P., & Ross, M. E. (2007). The origin of the Columbia River flood basalt province: Plume versus non-plume models. In G. R. Foulger & D. M. Jurdy (Eds.), *Special Paper 430: Plates, plumes and planetary processes* (pp. 635–668). Geological Society of America. https://doi.org/10.1130/2007.2430(30)
Houser, C., Masters, G., Shearer, P., & Laske, G. (2008). Shear and compressional velocity models of the mantle from cluster analysis of long-period waveforms. *Geophysical Journal International*, *174*(1), 195–212.
Hunt, S. A., Weidner, D. J., Li, L., Wang, L., Walte, N. P., Brodholt, J. P., & Dobson, D. P. (2009). Weakening of calcium iridate during its transformation from perovskite to post-perovskite. *Nature Geoscience*, *2*(11), 794–797.
Irifune, T., & Ringwood, A. E. (1993). Phase-transformations in subducted oceanic-crust and buoyancy relationships at depths of 600-800 km in the mantle. *Earth and Planetary Science Letters*, *117*(1-2), 101–110.
Jayananda, M., Kano, T., Peucat, J. J., & Channabasappa, S. (2008). 3.35 Ga komatiite volcanism in the western Dharwar craton, southern India: Constraints from Nd isotopes and whole-rock geochemistry. *Precambrian Research*, *162*(1-2), 160–179.
Jordan, T. H. (1978). Composition and development of the continental tectosphere. *Nature*, *274*(5671), 544–548.
Jordan, T. H. (1979). Mineralogies, densities and seismic velocities of garnet lherzolites and their geophysical implications. In F. R. Boyd & H. O. A. Meyer (Eds.), *The mantle sample: Inclusion in kimberlites and other volcanics* (Vol. 16, pp. 1–14). Washington, DC: American Geophysical Union.
Karato, S. i., & Wu, P. (1993). Rheology of the upper mantle: A synthesis. *Science*, *260*(5109), 771–778.
Kelemen, P. B., Hirth, G., Shimizu, N., Spiegelman, M., & Dick, H. J. (1997). A review of melt migration processes in the adiabatically upwelling mantle beneath oceanic spreading ridges. *Philosophical Transactions of the Royal Society of London Series a-Mathematical Physical and Engineering Sciences*, *355*(1723), 283–318.
Lay, T., Hernlund, J., & Buffett, B. A. (2008). Core-mantle boundary heat flow. *Nature Geoscience*, *1*(1), 25–32.

Lay, T., Hernlund, J., Garnero, E. J., & Thorne, M. S. (2006). A post-perovskite lens and D' heat flux beneath the central Pacific. *Science*, *314*(5803), 1272–1276.
Lee, C. T. A. (2003). Compositional variation of density and seismic velocities in natural peridotites at STP conditions: Implications for seismic imaging of compositional heterogeneities in the upper mantle. *Journal of Geophysical Research*, *108*(B9), 2441. https://doi.org/10.1029/2003JB002413
Lenardic, A., & Moresi, L. (2001). Heat flow scaling for mantle convection below a conducting lid: Resolving seemingly inconsistent modeling results regarding continental heat flow. *Geophysical Research Letters*, *28*(7), 1311–1314.
Lenardic, A., Moresi, L., Jellinek, A., & Manga, M. (2005). Continental insulation, mantle cooling, and the surface area of oceans and continents. *Earth and Planetary Science Letters*, *234*(3-4), 317–333.
Lenardic, A., Moresi, L., Jellinek, A. M., O'Neill, C. J., Cooper, C. M., & Lee, C. T. (2011). Continents, supercontinents, mantle thermal mixing, and mantle thermal isolation: Theory, numerical simulations, and laboratory experiments. *Geochemistry, Geophysics, Geosystems*, *12*, Q10016. https://doi.org/10.1029/2011GC003663
Leng, W., & Zhong, S. (2008). Controls on plume heat flux and plume excess temperature. *Journal of Geophysical Research*, *113*, B04408. https://doi.org/10.1029/2007JB005155
Li, X. D., & Romanowicz, B. (1996). Global mantle shear velocity model developed using nonlinear asymptotic coupling theory. *Journal of Geophysical Research*, *101*(B10), 22,245–22,272.
Lourenço, D. L., Rozel, A., & Tackley, P. J. (2016). Melting-induced crustal production helps plate tectonics on Earth-like planets. *Earth and Planetary Science Letters*, *439*, 18–28. https://doi.org/10.1016/j.epsl.2016.01.024
Lowman, J. P., & Gable, C. W. (1999). Thermal evolution of the mantle following continental aggregation in 3D convection models. *Geophysical Research Letters*, *26*(17), 2649–2652.
Lowman, J. P., & Jarvis, G. T. (1993). Mantle convection flow reversals due to continental collisions. *Geophysical Research Letters*, *20*(19), 2087–2090.
Lowman, J. P., & Jarvis, G. T. (1996). Continental collisions in wide aspect ratio and high Rayleigh number two-dimensional mantle convection models. *Journal of Geophysical Research*, *101*(B11), 25,485–25,497.
Marquart, G., Schmeling, H., & Braun, A. (1999). Small-scale instabilities below the cooling oceanic lithosphere. *Geophysical Journal International*, *138*(3), 655–666.
Masters, G., Laske, G., Bolton, H., & Dziewonski, A. (2000). The relative behavior of shear velocity, bulk sound speed, and compressional velocity in the mantle: Implications for chemical and thermal structure. In S. Karato, A. Forte, R. Liebermann, G. Masters, & L. Stixrude (Eds.), *Earth's deep interior: Mineral physics and tomography from the atomic to the global scale* (Vol. 117, pp. 63–87). Washington, DC: American Geophysical Union.
McKenzie, D., & Bickle, M. J. (1988). The volume and composition of melt generated by extension of the lithosphere. *Journal of Petrology*, *29*(3), 625–679.
Mittelstaedt, E., & Tackley, P. J. (2006). Plume heat flow is much lower than CMB heat flow. *Earth and Planetary Science Letters*, *241*(1-2), 202–210.
Mole, D. R., Fiorentini, M. L., Thébaud, N., Cassidy, K. F., McCuaig, T. C., Kirkland, C. L., & Miller, J. (2014). Archean komatiite volcanism controlled by the evolution of early continents. *Proceedings of the National Academy of Sciences*, *111*(28), 10,083–10,088.
Moresi, L., & Solomatov, V. (1998). Mantle convection with a brittle lithosphere: Thoughts on the global tectonic styles of the Earth and Venus. *Geophysical Journal International*, *133*(3), 669–682.
Morgan, W. J. (1972). Plate motions and deep mantle convection. In R. Shagam et al. (Eds.), *Studies in Earth and space sciences* (Vol. 132, pp. 7–22). Boulder, CO: Geological Society of America.
Nakagawa, T., & Tackley, P. J. (2004). Effects of thermo-chemical mantle convection on the thermal evolution of the Earth's core. *Earth and Planetary Science Letters*, *220*(1-2), 107–119.
Nakagawa, T., & Tackley, P. J. (2012). Influence of magmatism on mantle cooling, surface heat flow and Urey ratio. *Earth and Planetary Science Letters*, *329*, 1–10.
Nakagawa, T., Tackley, P. J., Deschamps, F., & Connolly, J. A. D. (2010). The influence of MORB and harzburgite composition on thermo-chemical mantle convection in a 3-D spherical shell with self-consistently calculated mineral physics. *Earth and Planetary Science Letters*, *296*(3-4), 403–412.
Neal, C. R., Mahoney, J. J., Kroenke, L. W., Duncan, R. A., & Petterson, M. G. (1997). The Ontong Java plateau. In J. Mahoney, & F. Coffin (Eds.), *Large igneous provinces: Continental, oceanic, and planetary flood volcanism* (Vol. 100, pp. 183–216). Washington, DC: American Geophysical Union.
Nisbet, E. G. (1982). The tectonic setting and petrogenesis of kamatiites. In N. T. Arnd & E. G. Nisbet (Eds.), *Komatiites* (pp. 501–520). London: George Allen & Unwin.
O'Neill, C., Lenardic, A., Jellinek, A. M., & Moresi, L. (2009). Influence of supercontinents on deep mantle flow. *Gondwana Research*, *15*(3-4), 276–287.
Ogawa, M. (2014). Two-stage evolution of the Earth's mantle inferred from numerical simulation of coupled magmatism-mantle convection system with tectonic plates. *Journal of Geophysical Research: Solid Earth*, *119*, 2462–2486. https://doi.org/10.1002/2013JB010315
Ono, S., Ito, E., & Katsura, T. (2001). Mineralogy of subducted basaltic crust (MORB) from 25 to 37 GPa, and chemical heterogeneity of the lower mantle. *Earth and Planetary Science Letters*, *190*(1-2), 57–63.
Panning, M., & Romanowicz, B. (2006). A three-dimensional radially anisotropic model of shear velocity in the whole mantle. *Geophysical Journal International*, *167*(1), 361–379.
Pearson, D. G., Parman, S. W., & Nowell, G. M. (2007). A link between large mantle melting events and continent growth seen in osmium isotopes. *Nature*, *449*(7159), 202–205.
Phillips, B., & Bunge, H. (2005). Heterogeneity and time dependence in 3D spherical mantle convection models with continental drift. *Earth and Planetary Science Letters*, *233*(1-2), 121–135.
Phillips, B. R., & Coltice, N. (2010). Temperature beneath continents as a function of continental cover and convective wavelength. *Journal of Geophysical Research*, *115*, B04408. https://doi.org/10.1029/2009JB006600
Pollack, H. N. (1986). Cratonization and thermal evolution of the mantle. *Earth and Planetary Science Letters*, *80*(1-2), 175–182.
Pozzo, M., Davies, C., Gubbins, D., & Alfè, D. (2013). Thermal and electrical conductivity of iron at Earth's core conditions. *Nature*, *485*(7398), 355–358.
Rampino, M. R., & Stothers, R. B. (1988). Flood basalt volcanism during the past 250 million years. *Science*, *241*(4866), 663–668.
Ricard, Y., Richards, M., Lithgow-Bertelloni, C., & Le Stunff, Y. (1993). A geodynamic model of mantle density heterogeneity. *Journal of Geophysical Research*, *98*(B12), 21,895–21,909.

Ricard, Y., Vigny, C., & Froidevaux, C. (1989). Mantle heterogeneities, geoid, and plate motion: A Monte Carlo inversion. *Journal of Geophysical Research*, *94*(B10), 13,739–13,754.
Richards, M. A., Duncan, R. A., & Courtillot, V. E. (1989). Flood basalts and hot-spot tracks: Plume heads and tails. *Science*, *246*(4926), 103–107.
Ritsema, J., Deuss, A., van Heijst, H. J., & Woodhouse, J. H. (2011). S40RTS: A degree-40 shear-velocity model for the mantle from new Rayleigh wave dispersion, teleseismic traveltime and normal-mode splitting function measurements. *Geophysical Journal International*, *184*(3), 1223–1236.
Ritsema, J., van Heijst, H. J., & Woodhouse, J. H. (1999). Complex shear wave velocity structure imaged beneath Africa and Iceland. *Science*, *286*(5446), 1925–1928.
Rolf, T., Coltice, N., & Tackley, P. J. (2012). Linking continental drift, plate tectonics and the thermal state of the Earth's mantle. *Earth and Planetary Science Letters*, *351-352*(C), 134–146.
Rolf, T., & Tackley, P. J. (2011). Focussing of stress by continents in 3D spherical mantle convection with self-consistent plate tectonics. *Geophysical Research Letters*, *38*, L18301. https://doi.org/10.1029/2011GL048677
Rozel, A. B., Golabek, G. J., Jain, C., Tackley, P. J., & Gerya, T. (2017). Continental crust formation on early Earth controlled by intrusive magmatism. *Nature*, *545*(7654), 332–335.
Rudnick, R. L., & Gao, S. (2003). Composition of the continental crust. In H. D. Holland & K. K. Turekian (Eds.), *Treatise on geochemistry* (Vol. 3, pp. 1–64). Amsterdam: Elsevier.
Schubert, G., Turcotte, D. L., & Olson, P. (2001). *Mantle convection in the Earth and planets*. Cambridge: Cambridge University Press.
Schutt, D. L., & Lesher, C. E. (2006). Effects of melt depletion on the density and seismic velocity of garnet and spinel lherzolite. *Journal of Geophysical Research*, *111*, B05401. https://doi.org/10.1029/2003JB002950
Scrutton, R. A. (1973). The age relationship of igneous activity and continental break-up. *Geological Magazine*, *110*(03), 227–234.
Sengör, A. M. C., & Burke, K. (1978). Relative timing of rifting and volcanism on Earth and its tectonic implications. *Geophysical Research Letters*, *5*(6), 419–421.
Solomatov, V. S. (1995). Scaling of temperature-dependent and stress-dependent viscosity convection. *Physics of Fluids*, *7*(2), 266–274.
Stevenson, D. J. (1990). Fluid dynamics of core formation. In H. E. Newsom & J. H. Jones (Eds.), *Origin of the Earth* (pp. 231–249). New York: Oxford University Press.
Su, W. J., & Dziewonski, A. M. (1997). Simultaneous inversion for 3-D variations in shear and bulk velocity in the mantle. *Physics of the Earth and Planetary Interiors*, *100*(1-4), 135–156.
Su, W. J., Woodward, R. L., & Dziewonski, A. M. (1994). Degree-12 model of shear velocity heterogeneity in the mantle. *Journal of Geophysical Research*, *99*(B4), 6945–6980.
Tackley, P. J. (2008a). Modelling compressible mantle convection with large viscosity contrasts in a three-dimensional spherical shell using the yin-yang grid. *Physics of the Earth and Planetary Interiors*, *171*(1-4), 7–18.
Tackley, P. J. (2008b). Self-consistent generation of tectonic plates in time-dependent, three-dimensional mantle convection simulations. *Geochemistry, Geophysics, Geosystems*, *1*, 1021. https://doi.org/10.1029/2000GC000036
Tackley, P. J., Ammann, M., Brodholt, J. P., Dobson, D. P., & Valencia, D. (2013). Mantle dynamics in super-Earths: Post-perovskite rheology and self-regulation of viscosity. *Icarus*, *225*(1), 50–61.
Tackley, P. J., & King, S. D. (2003). Testing the tracer ratio method for modeling active compositional fields in mantle convection simulations. *Geochemistry, Geophysics, Geosystems*, *4*(4), 8302. https://doi.org/10.1029/2001GC000214
van der Hilst, R. D., de Hoop, M. V., Wang, P., Shim, S. H., Ma, P., & Tenorio, L. (2007). Seismostratigraphy and thermal structure of Earth's core-mantle boundary region. *Science*, *315*(5820), 1813–1817.
van der Hilst, R. D., Widiyantoro, S., & Engdahl, E. R. (1997). Evidence for deep mantle circulation from global tomography. *Nature*, *386*(6625), 578–584.
Wang, Q., Schitte, L., & Campbell, I. H. (1996). Geochronological constraints on the age of komatiites and nickel mineralisation in the Lake Johnston Greenstone Belt, Yilgarn Craton, Western Australia. *Australian Journal of Earth Sciences*, *43*(4), 381–385.
White, R., & McKenzie, D. (1989). Magmatism at rift zones: The generation of volcanic continental margins and flood basalts. *Journal of Geophysical Research*, *94*(B6), 7685–7729.
Wooden, J. L., Czamanske, G. K., Fedorenko, V. A., Arndt, N. T., Chauvel, C., Bouse, R. M., & Siems, D. F. (1993). Isotopic and trace-element constraints on mantle and crustal contributions to Siberian continental flood basalts, Noril'sk area, Siberia. *Geochimica et Cosmochimica Acta*, *57*(15), 3677–3704.
Xie, S., & Tackley, P. J. (2004a). Evolution of helium and argon isotopes in a convecting mantle. *Physics of the Earth and Planetary Interiors*, *146*(3-4), 417–439.
Xie, S., & Tackley, P. J. (2004b). Evolution of U-Pb and Sm-Nd systems in numerical models of mantle convection and plate tectonics. *Journal of Geophysical Research*, *109*, B11204. https://doi.org/10.1029/2004JB003176
Xu, W., Lithgow-Bertelloni, C., Stixrude, L., & Ritsema, J. (2008). The effect of bulk composition and temperature on mantle seismic structure. *Earth and Planetary Science Letters*, *275*(1-2), 70–79.
Yamazaki, D., & Karato, S. i. (2001). Some mineral physics constraints on the rheology and geothermal structure of Earth's lower mantle. *American Mineralogist*, *86*(4), 385–391.
Yoshida, M., Iwase, Y., & Honda, S. (1999). Generation of plumes under a localized high viscosity lid in 3-D spherical shell convection. *Geophysical Research Letters*, *26*(7), 947–950.
Zerr, A., Diegeler, A., & Boehler, R. (1998). Solidus of Earth's deep mantle. *Science*, *281*(5374), 243–246.
Zhang, P., Cohen, R. E., & Haule, K. (2015). Effects of electron correlations on transport properties of iron at Earth's core conditions. *Nature*, *517*(7536), 605–607.
Zhao, D. P. (2004). Global tomographic images of mantle plumes and subducting slabs: Insight into deep Earth dynamics. *Physics of the Earth and Planetary Interiors*, *146*(1-2), 3–34.
Zhong, S. J. (2006). Constraints on thermochemical convection of the mantle from plume heat flux, plume excess temperature, and upper mantle temperature. *Journal of Geophysical Research*, *111*, B04409. https://doi.org/10.1029/2005JB003972
Zhong, S., & Gurnis, M. (1993). Dynamic feedback between a continentlike raft and thermal convection. *Journal of Geophysical Research*, *98*(B7), 12,219–12,232.
Zhong, S., & Liu, X. (2016). The long-wavelength mantle structure and dynamics and implications for large-scale tectonics and volcanism in the Phanerozoic. *Gondwana Research*, *29*(1), 83–104.
Zhong, S., Zhang, N., Li, Z. X., & Roberts, J. H. (2007). Supercontinent cycles, true polar wander, and very long-wavelength mantle convection. *Earth and Planetary Science Letters*, *261*(3-4), 551–564.

10.1029/2018GC007586

Erratum

In the originally published version of this article, Movies S1–S12 were not posted with the article. The article and the Supporting Information S1 file have since been corrected and the Supporting Information S1 file now reflects the correct movie names. This version may be considered the authoritative version of record.